Numerical Study on the Effect of Subcooling in Vapour Compression Refrigeration System Using Alternative Refrigerantse

Ranendra Roy (India), Bijan Kumar Mandal (india)

Abstract

Ozone depletion potential (ODP) and the global warming potential (GWP) play significant roles for selecting alternative to CFC and HCFC refrigerants. The discovery of ozone depletion properties of CFC and HCFC refrigerants leads to gradual phase out these refrigerants through Montreal protocol and Kyoto protocol. It has also been decided that the production and use of these refrigerants will finally be stopped by the end of 2030 throughout the world. So, it is necessary to find out environment friendly alternative to these refrigerants. Different researchers have suggested few HFC and HC refrigerants as suitable alternatives to CFC and HCFC refrigerants for the use in refrigeration and air conditioning industries. So, an attempt has been made to simulate vapour compression refrigeration system with these environment friendly refrigerants. A software based simulation of vapour compression refrigeration system has been carried out in this work using R152a, R404A, R507 and R600a as refrigerants. A computational simulation model is developed using CoolPack software and simulation is carried out for analyzing the performances of the vapour compression refrigeration system. The condenser temperature is varied from of 25^{o}C to 45^{o}C and evaporator temperature is varied from 0^{o}C to -20^{o}C during the simulation. Effect of compressor isentropic efficiency and degree of subcooling is also taken into consideration in the present work. The parameters that are computed in this study are compressor power, coefficient of performance (COP) and mass flow rate of refrigerants. Effect of sub-cooling on these computed parameters has also been studied. It is observed from the results that refrigerants R152a and R600a give better performance than other two refrigerants under investigation in all aspects. It is observed that compressor power is less while refrigerant R152a is used, whereas, that is high for refrigerant R404A. The compressor power for refrigerant R152a is 26.5% lower than that of refrigerant R404A. Compressor power required for refrigerant R600a is almost similar to R152a and it is only 6.6% higher than R152a. Refrigerants R152a and R600a give better COP than other two refrigerants. Refrigerant R152a gives the highest COP among the all. The difference in achieved COP between R152a and R600a is found to be 1.6%. The mass flow rate of refrigerant is also low when R152a and R600a are used as refrigerants. Mass flow rate is minimum with refrigerant R600a to get the same cooling effect and it is 3% lower from that with refrigerant R152a. The investigated parameters are also improved when subcooling is done. It is seen that when sub-cooling is done, mass flow rate of refrigerant, compressor power and COP of the system are improved.

Keywords: Alternative Refrigerants, R152a, R600a, COP, Sub-cooling, GWP, ODP

Available online at www.sciencedirect.com

ScienceDirect

Procedia Engineering00 (2015) 000–000

Procedia Engineering

www.elsevier.com/locate/procedia

6th BSME International Conference on Thermal Engineering (ICTE 2014)

Unsteady Flow through a Rotating Curved Channel with Rectangular Cross-Section

Md. Zohurul Islam[a,*], Rabindra Nath Mondal[b]

[a]*Dept. of Mathematics and Statistics, Jessore University of Science and Technology, Jessore-7408, Bangladesh*
[b]*Department of Mathematics, Jagannath University, Dhaka-1100, Bangladesh*

Abstract

A numerical study is presented for the fully developed two-dimensional thermal flow of viscous incompressible fluid through a rotating curved rectangular duct of constant curvature $\delta = 0.1$. In this paper, a spectral-based computational algorithm is employed as the principal tool for the simulations, while a Chebyshev polynomial, collocation method as secondary tools. Numerical calculations are carried out over a wide range of the Taylor number $0 \le Tr \le 2000$ and the Dean number $100 \le Dn \le 2000$ for the Grashof number $Gr = 500$. The outer wall of the duct is heated while the inner wall is cooled. Unsteady flow structures are examined for the effects of rotation parameter and pressure-driven parameter, and it is found that the unsteady flow undergoes in the scenario '*Chaotic* $\rightarrow$ *multi-periodic* $\rightarrow$ *periodic* $\rightarrow$ *steady-state*', if *Tr* is increased in the positive direction. Contours of secondary flow patterns, temperature profiles and axial flow distribution are also obtained at several values of *Tr*, and it is found that there exist two- and multi-vortex solutions. It is also found that the temperature distribution is consistent with the secondary and axial vortices, and convective heat transfer is significantly enhanced as the secondary vortices become stronger.

Peer-review under responsibility of organizing committee of the 6th BSMEInternational Conference on Thermal Engineering (ICTE 2014).

Keywords: Curved rectangular duct; secondary flow; unsteady solutions; Dean number and time evolution.

* Corresponding author. Tel.: +88-01717964452; fax: +88-042-161199.
*E-mail address:*mz.islam@just.edu.bd

Peer-review under responsibility of organizing committee of the 6th BSME International Conference on Thermal Engineering (ICTE 2014).

1. Introduction

Flow and heat transfer through curved ducts and channels have attracted much attention because of their ample applications in fluids engineering. Due to engineering applications and their intricacy, the flow in a rotating curved duct has become one of the most challenging research fields of fluid mechanics. Since rotating machines were introduced into engineering applications, such as in rotating systems, gas turbines, electric generators, heat exchangers, cooling systems and some separation processes, scientists have paid considerable attention to study the rotating curved duct flows. The readers are referred to Nandakumar and Masliyah [1], Ito [2] and Yanase *et al.* [3] for some outstanding reviews on curved duct flows.

Nomenclature

Dn	Dean number	w	Velocity components in the $z-$direction
Tr	Taylor number	x	Horizontal axis
Gr	Grashof number	y	Vertical axis
h	Half height of the cross section	z	Axis in the direction of the main flow
d	Half width of the cross section	λ	Resistance coefficient
L	Radius of the curvature	δ	Curvature of the duct
P_r	Prandtl number	μ	Viscosity
t	Time	υ	Kinematic
T	Temperature	ρ	Density
u	Velocity components in the $x-$direction	κ	Thermal diffusivity
v	Velocity components in the $y-$direction	ψ	Sectional stream function

The fluid flowing in a rotating curved duct is subjected to two forces: the *Coriolis force* due to rotation and the *centrifugal force* due to curvature. For isothermal flows of a constant property fluid, the Coriolis force tends to produce vortices while centrifugal force is purely hydrostatic. When a temperature induced variation of fluid density occurs for non-isothermal flows, both Coriolis and centrifugal type buoyancy forces can contribute to the generation of vortices. These two effects of rotation either enhance or counteract each other in a non-linear manner depending on the direction of wall heat flux and the flow domain. Therefore, the effect of system rotation is more subtle and complicated and yields new; richer features of flow and heat transfer in general, bifurcation and stability in particular, for non-isothermal flows. Selmi *et al.* [4] examined the combined effects of system rotation and curvature on the bifurcation structure of two-dimensional flows in a rotating curved duct with square cross section. Wang and Cheng [5], employing finite volume method, examined the flow characteristics and heat transfer in curved square ducts for positive rotation and found reverse secondary flow for the co-rotation cases. Selmi and Nandakumer [6] and Yamamoto *et al.* [7] performed studies on the flow in a rotating curved rectangular duct. When a temperature induced variation of fluid density occurs for non-isothermal flows, both Coriolis and centrifugal type buoyancy forces can contribute to the generation of vorticity (Mondal *et. al.*, [8]). These two effects of rotation either enhance or counteract each other in a non-linear manner depending on the direction of wall heat flux and the flow domain. Very recently, Mondal *et al.* [9] performed numerical investigation of the non-isothermal flows through a curved rectangular duct of large aspect ratio and obtained substantial results. Mondal *et al.* [10] also performed numerical investigation of the transient heat transfer and fluid flows through a rotating curved rectangular duct for the case of positive and negative rotation and obtained relevant results. However, there is no known study on the rotating curved rectangular channel flows in the presence of buoyancy force. The present paper is, therefore, an attempt to fill up this gap. Studying the effects of rotation on the flow unsteady characteristics, caused by the combined action of the centrifugal and coriolis force, is an important objective of the present study.

2. Mathematical Formulations

Consider a hydro-dynamically and thermally fully developed two-dimensional flow of viscous incompressible fluid through a rotating curved duct with rectangular cross section, whose height and wide are *2h* and *2l*, respectively. The coordinate system with the relevant notation is shown in Fig. 1, where *x′* and *y′* axes are taken to be in the horizontal and vertical directions respectively, and *z'* is the axial direction. The system rotates at a constant angular velocity Ω_T around the *y′* axis. It is assumed that the outer wall of the duct is heated while the inner wall is cooled. The temperature of the outer wall is $T_0 + \Delta T$ and that of the inner wall is $T_0 - \Delta T$, where $\Delta T > 0$. The *x*, *y* and *z* axes are taken to be in the modified horizontal, vertical, and axial directions respectively. It is assumed that the flow is uniform in the axial direction, which is driven by a constant pressure gradient *G* along the central-line of the duct as shown in Fig. 1. The variables are non-dimensionalized by using the representative length l and the representative velocity U_0 .

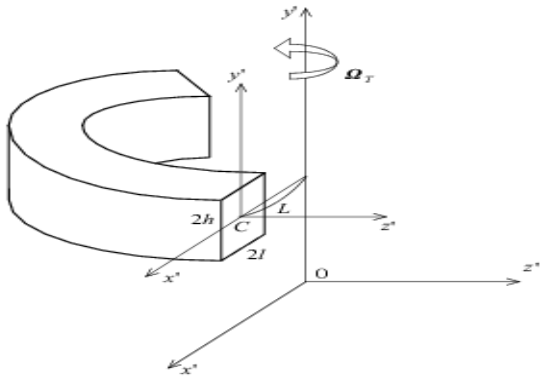

Fig. 1. Coordinate system of the rotating curved duct.

Since the flow field is uniform in the z direction, the sectional stream function ψ is introduced as,

$$u = \frac{1}{1+\delta x}\frac{\partial \psi}{\partial y}, \quad v = -\frac{1}{1+\delta x}\frac{\partial \psi}{\partial x}. \tag{1}$$

A new coordinate variable y' is introduced in the y direction as $y = ay'$, where $a = h/d$ is the aspect ratio of the duct cross section. From now on y denotes y' for the sake of simplicity. Then the basic equations for the axial velocity *w*, the stream function ψ and the temperature *T* are derived from the Navier-Stokes equations and the energy equation under the *Boussinesq approximation* as,

$$(1+\delta x)\frac{\partial w}{\partial t} + \frac{1}{a}\frac{\partial (w,\psi)}{\partial (x,y)} - Dn + \frac{\delta^2 w}{1+\delta x} = (1+\delta x)\Delta_2 w - \frac{1}{a}\frac{\delta}{(1+\delta x)}\frac{\partial \psi}{\partial y}w + \delta\frac{\partial w}{\partial x} - \delta Tr\frac{\partial \psi}{\partial y} \tag{2}$$

$$\left(\Delta_2 - \frac{\delta}{1+\delta x}\frac{\partial}{\partial x}\right)\frac{\partial \psi}{\partial t} = -\frac{1}{a}\frac{1}{(1+\delta x)}\frac{\partial (\Delta_2\psi,\psi)}{\partial (x,y)} + \frac{1}{a}\frac{\delta}{(1+\delta x)^2}\times\left[\frac{\partial \psi}{\partial y}\left(2\Delta_2\psi - \frac{3\delta}{1+\delta x}\frac{\partial \psi}{\partial x} + \frac{\partial^2 \psi}{\partial x^2}\right)\right.$$

$$\left. - \frac{\partial \psi}{\partial x}\frac{\partial^2 \psi}{\partial x \partial y}\right] + \frac{\delta}{(1+\delta x)^2}\times\left[3\delta\frac{\delta^2 \psi}{\partial x^2} - \frac{3\delta^2}{1+\delta x}\frac{\partial \psi}{\partial x}\right] - \frac{2\delta}{1+\delta x}\frac{\partial}{\partial x}\Delta_2\psi + \frac{1}{a}w\frac{\partial w}{\partial y} + \Delta_2^2\psi$$

$$- Gr(1+\delta x)\frac{\partial T}{\partial x} - \frac{1}{2}Tr\frac{\partial w}{\partial y}, \tag{3}$$

$$\frac{\partial T}{\partial t} + \frac{1}{(1+\delta x)}\frac{\partial (T,\psi)}{\partial (x,y)} = \frac{1}{\mathrm{Pr}}\left(\Delta_2 T + \frac{\delta}{1+\delta x}\frac{\partial T}{\partial x}\right) \tag{4}$$

where, $\Delta_2 \equiv \frac{\partial^2}{\partial x^2} + \frac{1}{a^2}\frac{\partial^2}{\partial y^2}$, $\frac{\partial(f,g)}{\partial(x,y)} \equiv \frac{\partial f}{\partial x}\frac{\partial g}{\partial y} - \frac{\partial f}{\partial y}\frac{\partial g}{\partial x}$

The non-dimensional parameters Dn, the Dean number, Tr, the Taylor number, Gr, the Grashof number and Pr, the prandtl number, which appear in equations (2) to (4) are defined as:

$$Dn = \frac{Gl^3}{\mu\upsilon}\sqrt{\frac{2l}{L}}, \quad Tr = \frac{2\sqrt{2\delta}\Omega_T l^3}{\upsilon\delta}, \quad Gr = \frac{\beta g \Delta T l^3}{\upsilon^2}, \quad \Pr = \frac{\upsilon}{\kappa} \tag{5}$$

where μ, β, κ and g are the coefficient of viscosity, the coefficient of thermal expansion, the co-efficient of thermal diffusivity and the gravitational acceleration respectively, υ is the viscosity of the fluid. In the present study, Dn and Tr are varied while Gr, a, δ and Pr are fixed as Gr =500, a = 2, $\delta = 0.1$ and $\Pr = 0.71$ (Air).
The rigid boundary conditions for w and ψ are used as

$$w(\pm1, y) = w(x, \pm1) = \psi(\pm1, y) = \psi(x, \pm1) = \frac{\partial\psi}{\partial x}(\pm1, y) = \frac{\partial\psi}{\partial y}(x, \pm1) = 0 \tag{6}$$

and the temperature T is assumed to be constant on the walls as

$$T(1, y) = 1, \quad T(-1, y) = -1, \quad T(x, \pm1) = x \tag{7}$$

3. Numerical Methods

In order to solve the Equations (2) to (4) numerically, the spectral method is used. By this method the expansion functions $\phi_n(x)$ and $\psi_n(x)$ are expressed as

$$\left.\begin{aligned} \phi_n(x) &= (1-x^2)C_n(x), \\ \psi_n(x) &= (1-x^2)^2 C_n(x) \end{aligned}\right\} \tag{8}$$

where $C_n(x) = \cos\left(n\cos^{-1}(x)\right)$ is the n^{th} order Chebyshev polynomial. $w(x,y,t)$, $\psi(x,y,t)$ and $T(x,y,t)$ are expanded in terms of the expansion functions $\phi_n(x)$ and $\psi_n(x)$ as

$$\left.\begin{aligned} w(x,y,t) &= \sum_{m=0}^{M}\sum_{n=0}^{N} w_{mn}(t)\varphi_m(x)\varphi_n(y) \\ \psi(x,y,t) &= \sum_{m=0}^{M}\sum_{n=0}^{N} \psi_{mn}(t)\psi_m(x)\psi_n(y). \\ T(x,,y,t) &= \sum_{m=0}^{M}\sum_{n=0}^{N} T_{mn}\varphi_m(x)\varphi_n(y) + x \end{aligned}\right\} \tag{9}$$

where M and N are the truncation numbers in the x and y directions respectively. The accuracy of the numerical calculations is investigated for the truncation numbers M and N used in this study. Five types of grid sizes were used to check the dependence of grid size (i.e. M and N). For good accuracy of the solutions, N is chosen equal to $2M$. The grid sizes are taken as 14×28, 16×32, 18×36, 20×40, 22×44, and it is found that M = 16 and N = 32 give sufficient accuracy of the numerical solutions, which are not shown here for brevity. In order to calculate the unsteady solutions, the Crank-Nicolson and Adams-Bashforth methods together with the function expansion (9) and the collocation methods are applied to Eqs. (2) to (4).

4. Resistance coefficient

We use the resistance coefficient λ as one of the representative quantities of the flow state. It is also called the *hydraulic resistance coefficient*, and is generally used in fluids engineering, defined as,

$$\frac{P_1^* - P_2^*}{\Delta z^*} = \frac{\lambda}{dh^*}\frac{1}{2}\rho\left\langle w^* \right\rangle^2, \tag{10}$$

where quantities with an asterisk denote the dimensional ones, $\langle\,\rangle$ stands for the mean over the cross section of the rectangular duct, and $d_h^* = 4(2l\times 4lh)/(4l\times 8lh)$. Since $\left(P_1^* - P_2^*\right)/\Delta z^* = G$, λ is related to the mean non-dimensional axial velocity $\langle w\rangle$ as $\lambda = \dfrac{16\sqrt{2\delta}Dn}{3\langle w\rangle^2}$, (11)

where $\langle w\rangle = \sqrt{2\delta}d/\nu\left\langle w^* \right\rangle$. In this paper, λ is used to calculate the unsteady solutions by numerical computations.

5. Results and Discussion

We take a curved rectangular duct of aspect ratio 2 and curvature $\delta = 0.1$ and rotate it around the centre of curvature with an angular velocity Ω_T in the positive direction. In this paper, time evolution calculations of the resistant coefficient λ are performed for the non-isothermal flows (Gr = 500) over a wide range of the Dean Numbers (*Dn*) and the Taylor Number (*Tr*) for the two cases of the duct rotation, *Case I*: *Dn* = 500 and *Case II*: *Dn* = 1000.

5.1 Case I: Dean Number, Dn=500

For positive rotation we perform time evolution of λ for $0 \le Tr \le 2000$ and $100 \le Dn \le 1000$. Fig. 2(a) shows time evolution of λ for Tr = 100 and Dn = 500 at Gr = 500. It is found that the unsteady flow at Tr = 100 is a chaotic solution, which is well justified by drawing the phase space as shown in Fig. 2(b). Fig. 2(c) shows typical contours of secondary flow patterns, temperature profiles and axial flow for Tr = 100 and Dn = 500, where we find that the unsteady flow is a two and four-vortex solution. This is caused by the combined action of the Coriolis force and centrifugal force, which increased the number of secondary vortices (Wang and Cheng [5]). To draw the contours of secondary flow (ψ), axial flow (w) and temperature profiles (T) for the curved rectangular channel, we use the increments $\Delta\psi = 0.6$, $\Delta w = 12$ and ΔT = 0.2, respectively. The same increments of ψ, w and T are used for all the figures in this study unless specified. The right-hand side of each channel box of ψ, w and T is in the outside direction of the duct curvature. In the figures of the secondary flows, solid lines ($\psi \ge 0$) show that the secondary flow is in the counter clockwise direction while the dotted lines $(\psi < 0)$ in the clockwise direction. Similarly in the figures of the temperature field, solid lines are those for $T \ge 0$ and dotted ones for T< 0. Then we perform time evolution of λ for Tr = 500 as shown in Fig. 3(a). It is found that the unsteady flow is a weak chaotic solution. In order to observe the chaotic oscillation more clearly, we draw the phase space of the time evolution result as shown in Fig. 3(b), and it is found that the flow oscillates in the irregular pattern, which confirms that the flow is chaotic. Typical contours of secondary flow patterns and temperature profiles are shown in Fig. 3(c), and we see that the unsteady flow is a two and four-vortex solution. Then we perform time evolution of λ for Tr = 555 as shown in Fig. 4(a). It is found that the unsteady flow at Tr = 555 is a multi-periodic solution, which is well justified by drawing the phase space as shown in Fig. 4(b). As seen in Fig. 4(b), the flow creates multiple orbits in its path, so that the unsteady flow at Tr = 555 is a multi-periodic solution. Typical contours of secondary flow patterns and temperature profiles for the corresponding flow parameters are shown in Fig. 4(c), where it is found that the multi-periodic oscillation at Tr = 555 is a two-vortex solution. Then we perform time evolution of λ for Tr = 557 as shown in Fig. 5(a). It is found that the unsteady flow at Tr = 557 is a multi-periodic solution, which is well justified by drawing the phase space as shown in Fig. 5(b). As seen in Fig. 5(b), the flow creates single orbits in its path, so that the unsteady flow at Tr = 557 is a periodic solution. Typical contours of secondary flow patterns and temperature profiles for the corresponding flow parameters are shown in Fig. 5(c), where it is found that the multi-periodic oscillation at Tr = 557 is a two-vortex solution. If the rotational speed is increases more in the positive direction, for example Tr = 558 up to 2000, it is found that the flow becomes steady-state which is shown in figure 6(a) for Tr = 2000. Since the unsteady flow is a steady-state solution, a single contour of secondary flow pattern and

temperature profile is shown in Fig. 6(b), and it is found that steady-state solution is a two-vortex flow.

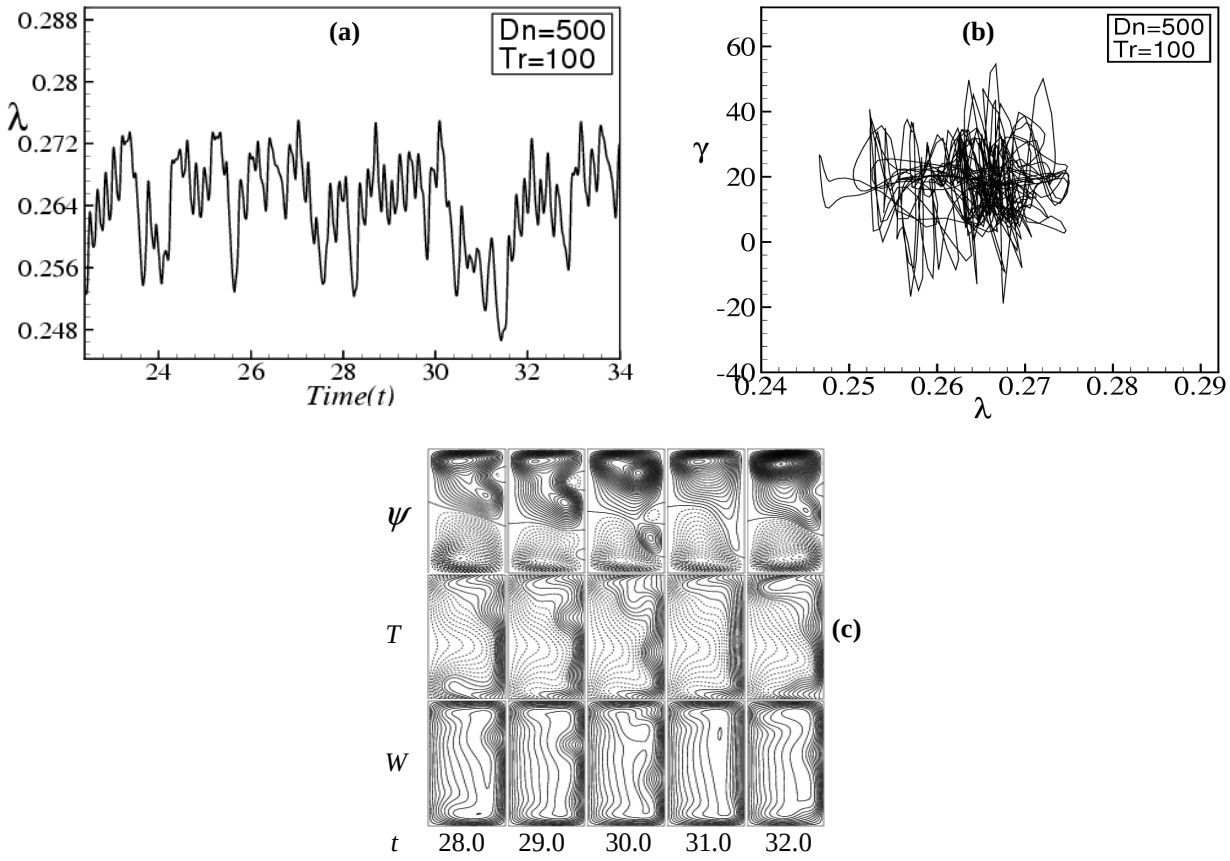

Fig. 2. (a) Time evolution of λ for Dn = 500 and Tr = 100. (b) Phase space for Tr =100, (c) Contours of secondary flow patterns (top) temperature profiles (middle) and axial flow (bottom) for Tr = 100, at time $28.0 \le t \le 32.0$.

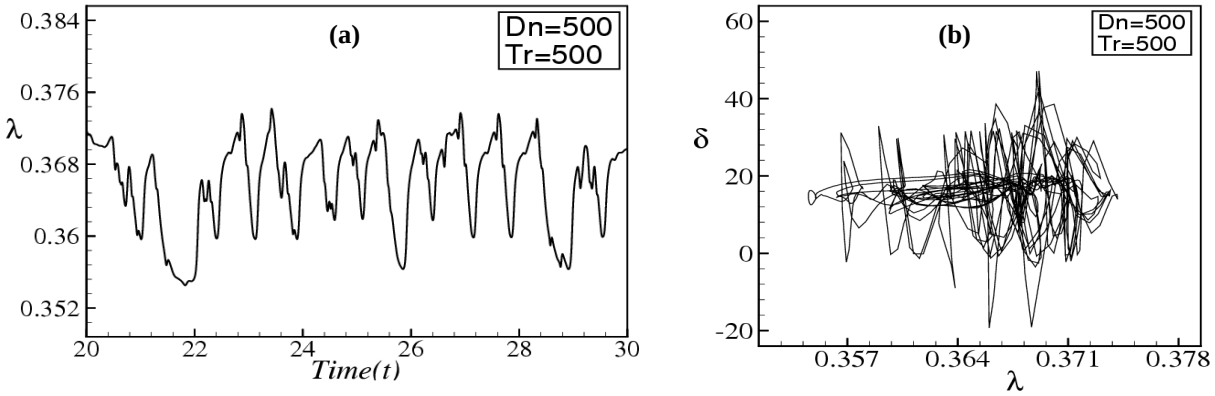

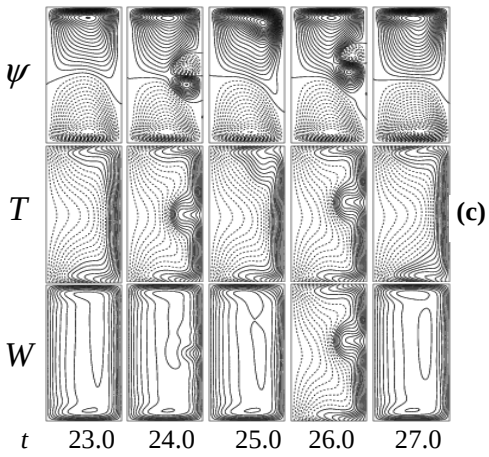

Fig. 3. (a) Time evolution of λ for Dn = 500 and Tr = 500. (b) Phase space for Tr =500, (c) Contours of secondary flow patterns (top) temperature profiles (middle) and axial flow (bottom) for Tr = 500, at time $23.0 \leq t \leq 27.0$.

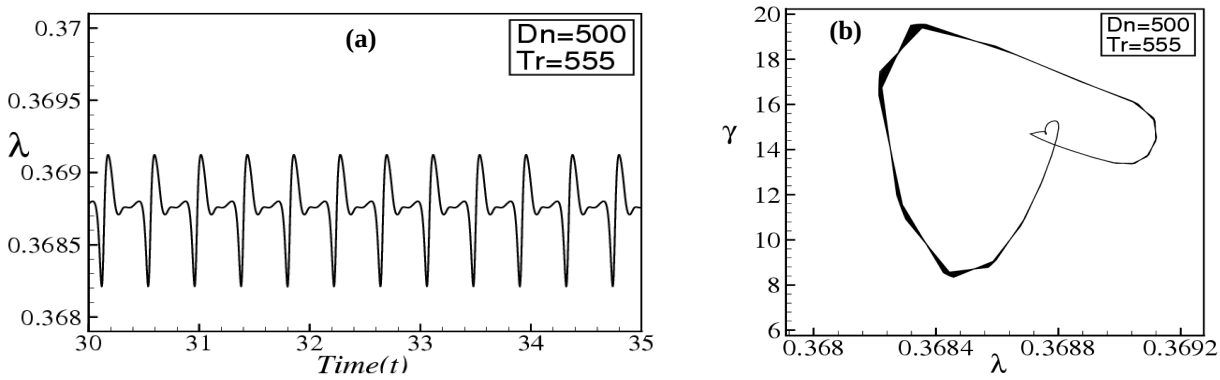

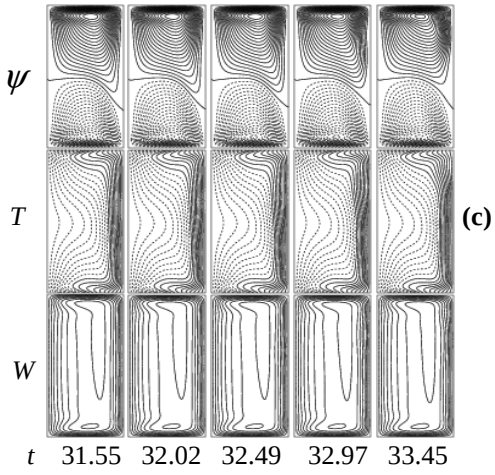

Fig. 4. (a) Time evolution of λ for Dn = 500 and Tr = 555. (b) Phase space for Tr = 555, (c) Contours of secondary flow patterns (top) temperature profiles (middle) and axial flow (bottom) for Tr = 555, at time $31.55 \leq t \leq 33.45$.

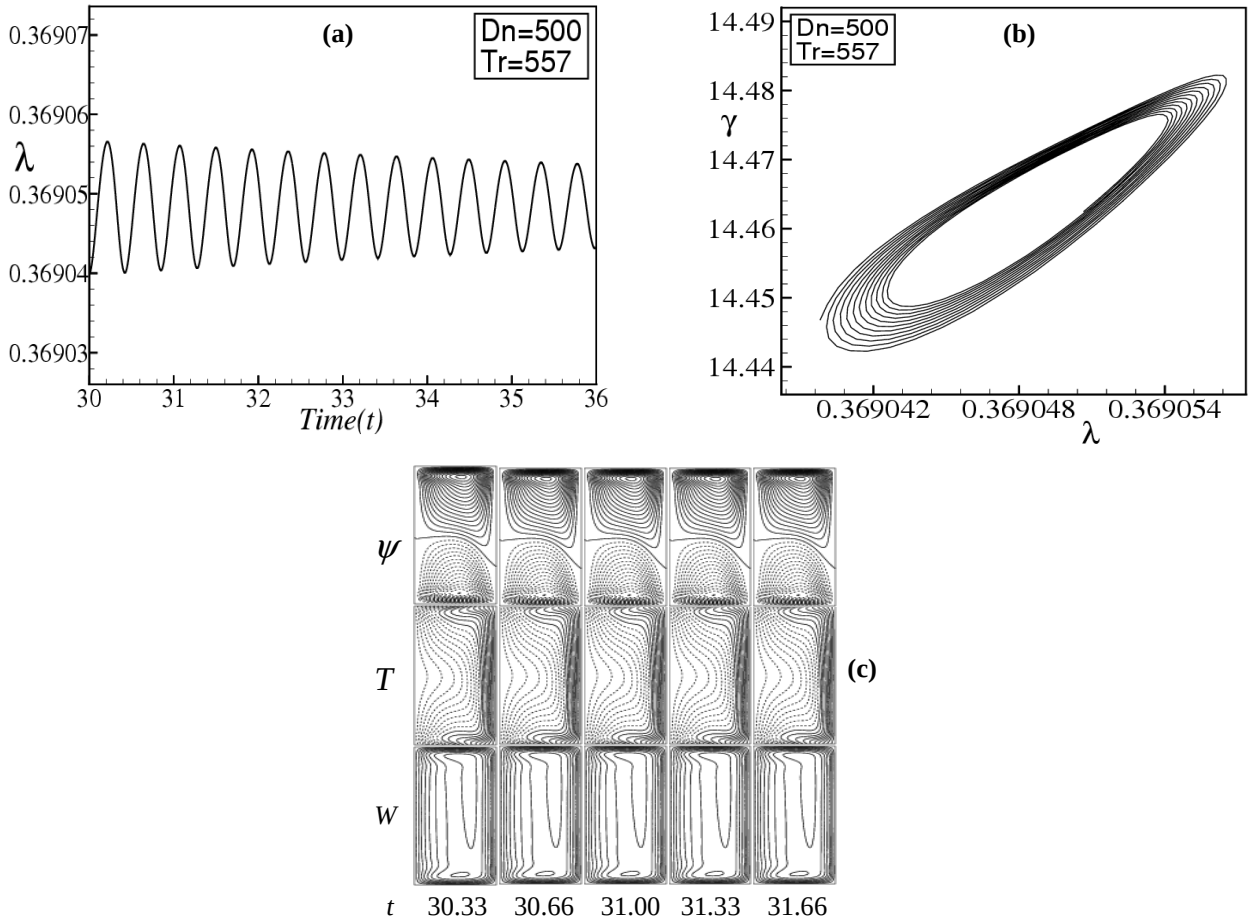

Fig. 5. (a) Time evolution of λ for Dn = 500 and Tr = 557. (b) Phase space for Tr = 557, (c) Contours of secondary flow patterns (top) temperature profiles (middle) and axial flow (bottom) for Tr = 557, at time $30.55 \leq t \leq 31.66$.

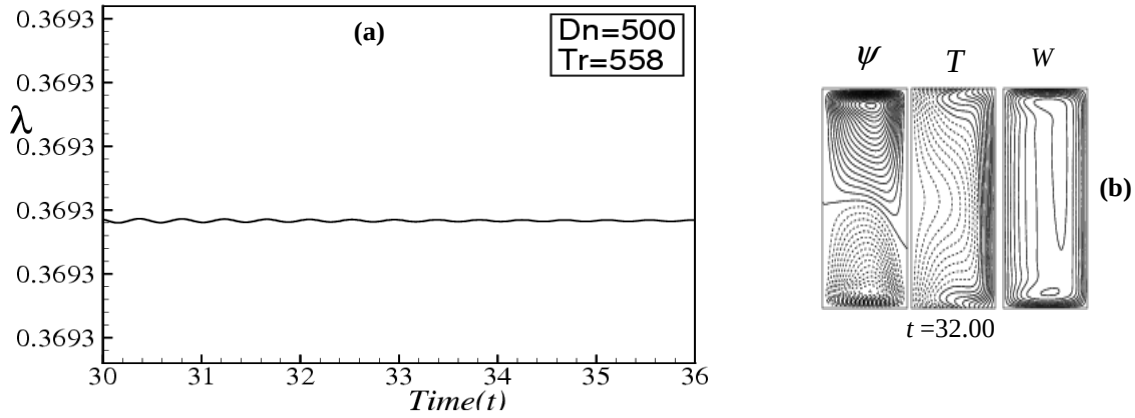

Fig. 6. (a) Time evolution of λ for Dn = 500 and Tr = 558. (b) Contours of secondary flow patterns (top) temperature profiles (middle) and axial flow (bottom) for Tr = 558 at time $t = 33.00$.

5.2 Case II: Dean Number, Dn=1000

We perform time evolution of λ for $0 \le Tr \le 2000$ and $Dn = 1000$ for $\delta = 0.1$. Fig. 7(a) shows time evolution of λ for Dn = 1000 and Tr = 100 at Gr = 500. It is found that the unsteady flow at Tr = 100 is a strongly chaotic solution, which is well justified by drawing the phase space as shown in Fig. 7(b). Fig. 7(c) shows typical contours of secondary flow patterns and temperature profiles for Tr = 100, where we find that the unsteady flow is a six-vortex solution. Then we perform time evolution of λ for Tr = 1500 and 1560 and presented in Figs. 8(a) and 9(a), respectively. It is found that the unsteady flow is multi-periodic oscillation for both at Tr = 1500 and Tr = 1560. The multi-periodic oscillations are well justified by depicting the phase spaces as shown in Figs. 8(b) and 9(b) for Tr = 1500 and Tr = 1560 respectively. In Figs. 8(b) and 9(b) the multi-periodic orbits of the time evolution solutions are seen, which proves that the oscillation presented in Figs. 8(b) and 9(a) are multi-periodic. Typical contours of secondary flow patterns, temperature profiles and axial flow are shown in Figs. 8(c) and 9(c) for Tr = 1500 and Tr = 1560 respectively. It is found that the multi-periodic solutions are four and two-vortex solutions respectively. If the rotational speed is increased more, for example Tr = 1565 or more, it is found that the flow becomes steady-state. Figure 10(a) shows time evolution of λ for Tr = 1565 and Dn = 1000, and it is found that the flow is steady-state. Since the flow is steady-state, a single contour of secondary flow pattern and temperature profile is shown in Fig. 10(b) for Tr = 1665 and Dn = 1000, and it is found that the unsteady flow for Tr = 1565 and Dn = 1000 is an asymmetric two-vortex solution. In this study, it is found that combined action of the coriolis and centrifugal force help to increase the number of secondary vortices. It is also found that, as the flow becomes chaotic, the secondary flow increases and gets stronger and consequently heat is transferred substantially.

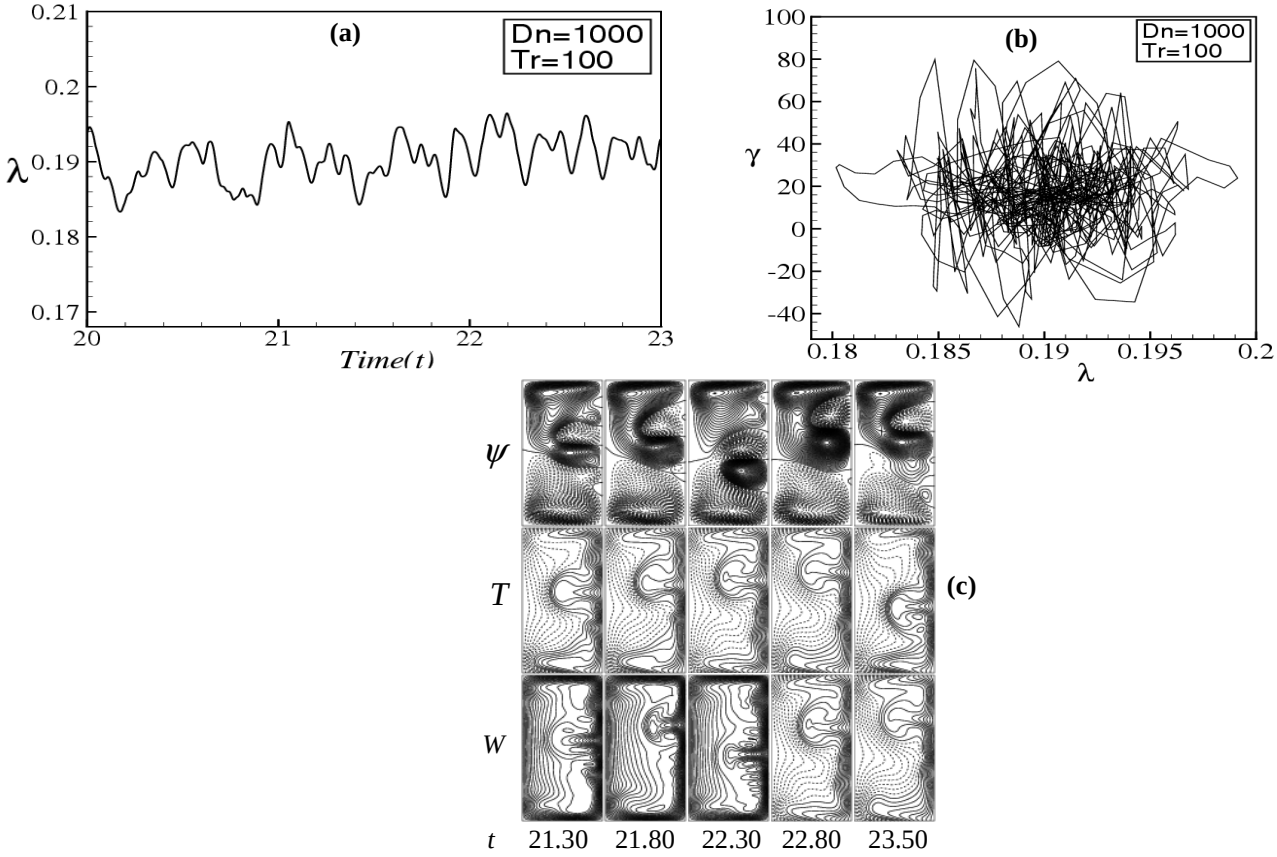

Fig. 7. (a) Time evolution of λ for Tr = 100 and Dn = 1000 at Gr = 500. (b) Phase space for Tr = 100. (c) Contours of secondary flow patterns (top) temperature profiles (middle) and axial flow (bottom) for Tr = 100, $21.30 \le t \le 23.50$.

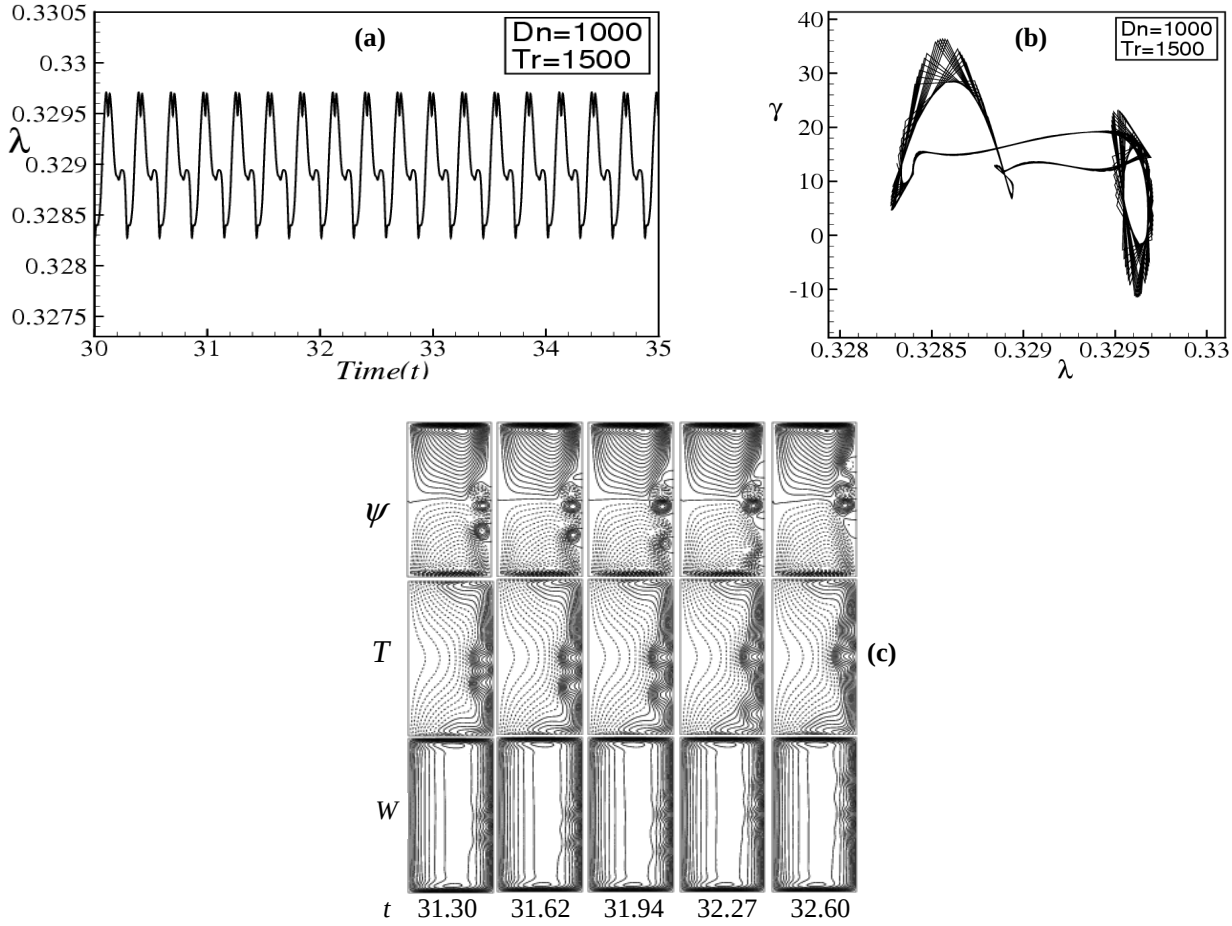

Fig. 8. (a) Time evolution of λ for Tr = 1500 and Dn = 1000 at Gr = 500. (b) Phase space for Tr = 1500. (c) Contours of secondary flow patterns (top) temperature profiles (middle) and axial flow (bottom) for Tr = 1500, $31.30 \leq t \leq 32.60$.

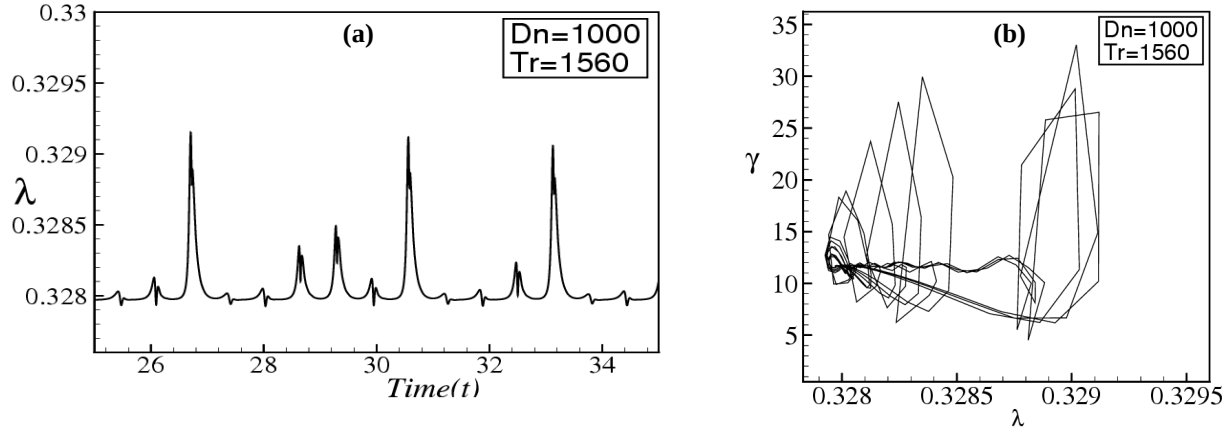

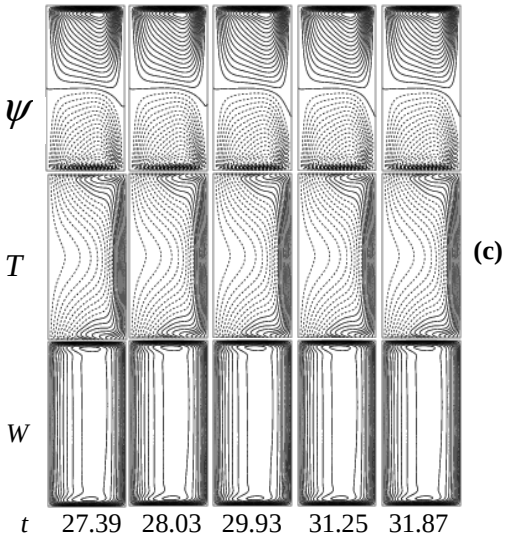

Fig. 9. (a) Time evolution of λ for Tr = 1560 and Dn = 1000 at Gr = 500. (b) Phase space for Tr = 1560. (c) Contours of secondary flow patterns (top) temperature profiles (middle) and axial flow (bottom) for Tr = 1560, $27.39 \le t \le 31.87.$

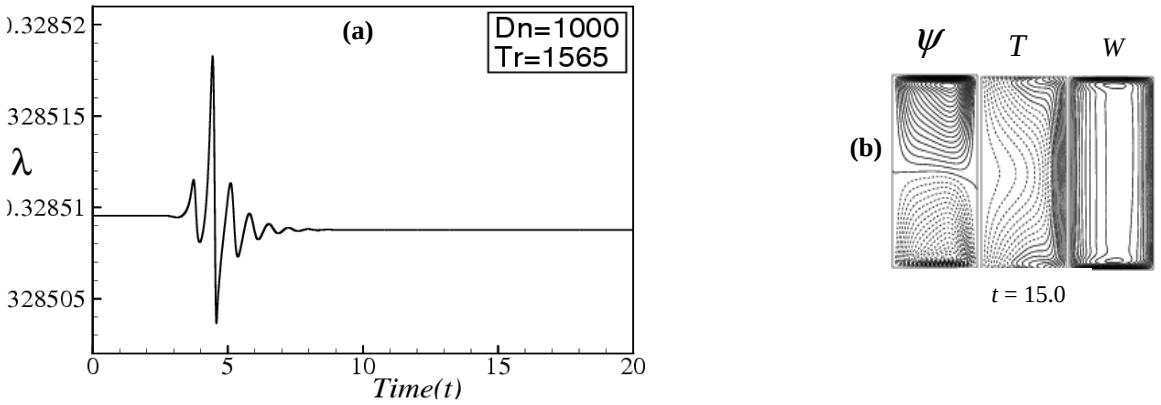

Fig. 10. (a) Time evolution of λ for Dn = 1000 and Tr = 1565. (b) Contours of secondary flow patterns (first) temperature profiles (second) and axial flow (third) for Tr = 1565 at time $t = 15.0$

6. Conclusion

A numerical study is presented for the flow characteristics through a rotating curved rectangular duct of aspect ratio 2 and curvature $\delta = 0.1$. Numerical calculations are carried out by using a spectral method, and covering a wide range of the Taylor number $0 \le Tr \le 2000$ for the Dean numbers, Dn = 500 and Dn = 1000 for the Grashof number $Gr = 500$. We investigated unsteady flow characteristics for the positive rotation of the duct by time evolution calculations, and it is found that the unsteady flow undergoes in the scenario '*Chaotic* $\rightarrow$ *multi-periodic* $\rightarrow$ *periodic* $\rightarrow$ *steady-state'*, if *Tr* is increased in the positive direction. Phase spaces were found to be fruitful to justify the transition of unsteady flow characteristics. Typical contours of secondary flow patterns and temperature profiles are also obtained at several values of *Tr*, and it is found that there exist two-, four- and six-vortex solutions if the duct rotation involved in the positive direction. It is found that the temperature distribution is consistent with the secondary vortices, and convective heat transfer is enhanced as the secondary vortices increase. It is also found that chaotic flow enhances heat transfer more significantly than the periodic or steady-state solutions.

References

[1] Nandakumar, K. and Masliyah, J. H. (1986). Swirling Flow and Heat Transfer in Coiled and Twisted Pipes, *Adv. Transport Process*., Vol. **4**, pp. 49-112.

[2] Ito, H (1987). Flow in curved pipes. *JSME International Journal*, **30**, 543–552.

[3] Yanase, S., Kaga, Y. and Daikai, R. (2002). Laminar flow through a curved rectangular duct over a wide range of the aspect ratio, *Fluid Dynamics Research*, Vol. **31,** pp. 151-183.

[4] Selmi, M. and Namdakumar, K. and Finlay W. H., 1994. A bifurcation study of viscous flow through a rotating curved duct, *J. Fluid Mech.* Vol. **262**, pp. 353-375.

[5] Wang, L. Q. and Cheng, K.C., 1996. Flow Transitions and combined Free and Forced Convective Heat Transfer in Rotating Curved Channels: the Case of Positive Rotation Physics *of Fluids*, Vol. **8**, pp.1553-1573.

[6] Selmi, M. and Namdakumar, K. (1999). Bifurcation Study of the Flow through Rotating Curved Ducts, *Physics of Fluids*, Vol. **11**, pp. 2030-2043.

[7] Yamamoto, K., Yanase, S. and Alam, M. M. (1999). Flow through a Rotating Curved Duct with Square Cross-section, *J. Phys. Soc*. Japan, Vol. **68**, pp. 1173-1184.

[8] Mondal, R. N., Alam M. M. and Yanase, S. (2007). Numerical prediction of non- isothermal flows through a rotating curved duct with square cross section, *Thommasat Int. J. Sci and Tech.*, Vol. **12**, No. 3, pp. 24-43.

[9] Mondal, R. N., Datta, A. K. and Uddin, M. K. (2012). A Bifurcation Study of Laminar Thermal Flow through a Rotating Curved Duct with Square Cross-section, *Int. J. Appl. Mech. and Engg.* Vol. **17** (2). (In Press).

[10] Mondal, R. N., Md. Zohurul Islam and Md. Saidul Islam. (2013). Transient Heat and Fluid Flow through a Rotating Curved Rectangular Duct: The Case of Positive and Negative Rotation, *Procedia Engineering, Elsevier*. Vol. **56,** No. 2, pp. 179-186.

Available online at www.sciencedirect.com

ScienceDirect

Procedia Engineering 00 (2015) 000–000

Procedia Engineering

www.elsevier.com/locate/procedia

6th BSME International Conference on Thermal Engineering (ICTE 2014)

Experimental Study on Temperature Separation in Vortex Chamber

Shigeru Matsuo[a,*], Yuhi Matsuno[b], Yusuke Fukushima[b], Mohammad Mamun[c], Tokitada Hashimoto[a], Toshiaki Setoguchi[d], Heuy Dong Kim[e]

[a]*Department of Advanced Technology Fusion, Saga University, 1 Honjo-machi, Saga 840-8502, Japan*
[b]*Graduate School of Science & Engineering, Saga University, 1 Honjo-machi, Saga-shi, Saga 840-8502, Japan*
[c]*Department of Mechanical Engineering, Bangladesh University of Engineering & Technology, Dhaka 1000, Bangladesh*
[d]*Institute of Ocean Energy, Saga University, 1 Honjo-machi, Saga-shi, Saga 840-8502, Japan*
[e]*School of Mechanical Engineering, Andong National University, 388 Song Cheon Dong, Andong 760-749, Korea*

Abstract

It is known in the previous researches that the swirl flow in circular pipe causes the temperature separation. Recently, it is shown that the temperature separation occurs in a chamber composed by cylindrical vortex chamber, tangential pipe, the central rod and discharge collector. In this device, high and low temperature regions occur in a cavity on the circumference of the chamber and center in vortex chamber, respectively. The highest temperature was observed in the bottom of the cavity. Therefore, it is expected that this device can be used as a heat source in the engineering field. In recent researches, the mechanism of temperature separation in the vortex chamber has been investigated experimentally and numerically by some researchers. However, there are few researches for the effect of configuration and position of the cavity on the temperature separation. In the present study, the effects of configuration of vortex chamber including a cavity and cavity position on temperature separation in the vortex chamber were investigated experimentally.

Peer-review under responsibility of organizing committee of the 6th BSME International Conference on Thermal Engineering (ICTE 2014).

Keywords: Vortex chamber ; temperature separation ; cavity flow ; compressible flow ; oscillation.

* Corresponding author. Tel.: +81-952-28-8606; fax: +81-952-28-8687.
E-mail address: matsuo@me.saga-u.ac.jp

Peer-review under responsibility of organizing committee of the 6th BSME International Conference on Thermal Engineering (ICTE 2014).

1. Introduction

Nomenclature

A	cross section (mm^2)
d	diameter (mm)
D	vortex chamber diameter (mm)
D_c	cavity depth (mm)
H	height of vortex chamber (mm)
h	height of central rod from base wall (mm)
p	static pressure (MPa)
t	time (s)
T	temperature (K)
Subscripts	
0	stagnation point
a	atmosphere
c	cavity
exit	air collector exit
out	vortex chamber exit
r	rod

In the previous researches, it is known that the swirl flow in circular pipe leads to the temperature separation [1-3]. Recently, it was clarified that the temperature separation occurs in a vortex chamber [4-6] composed by cylindrical chamber, tangential pipe, the central rod and discharge collector when compressed air are pumped into this device from the circumference. Especially, in a cavity installed in the circumference of vortex chamber, the large temperature increase was observed and the lowest temperature was obtained in the chamber central zone. Therefore, it is expected that this device can be used as a heat source in the engineering field. In Ref.[7], it is known that the temperature separation is affected by the exit cross section ratio (the ratio of the discharge collector cross section to vortex chamber outlet cross section). Some researchers have investigated the mechanism of temperature separation in vortex chamber [5-7]. However, there are few for researches of the effect of the position and depth of cavity on the temperature separation. Further, physical explanation has not been almost made for the temperature separation phenomena in the vortex chamber.

In the present study, the effects of configuration of chamber including a cavity and cavity position on temperature separation in the vortex chamber are investigated experimentally and the cause of temperature increase and flow behavior in the vortex chamber is considered from the point of view of pressure oscillation.

2. Experimental setup and procedure

Figure 1 shows a schematic diagram of the experimental apparatus. The apparatus is consisted of compressor, air drier, air reservoir, electronic control valve, plenum chamber and vortex chamber. Dry air was used as the working gas, and the compressed air in the plenum chamber was controlled by electronic control valve.

Figure 2 shows details of vortex chamber. The configuration proposed by Beliavsky [1] was used in the present study. The vortex chamber is composed of the cylindrical vortex chamber, four tangential pipes (inside diameter : 5 mm) mounted on the circumference of the vortex chamber, the central rod and discharge collector which are installed coaxial to the vortex chamber. Diameter and height of the cylindrical vortex chamber are set at D =140 mm, H= 25 mm, respectively. The rod is d_r=15 mm in diameter. Diameter of a cavity was set at d_c=8 mm and its depth D_c was set at 4 mm, 8 mm, 16 mm and 32 mm.

In the present experiment, pressure ratio p_0/p_a is gradually increased from 1 to 6 by 1. p_0 and p_a are stagnation pressure of the plenum chamber and atmospheric pressure, respectively. Atmospheric pressure p_a is 101.2 kPa and atmospheric temperature T_a is 299 K. The temperature and pressure in vortex chamber were measured by sheathed thermocouple (CHINO SUS316) and pressure transducer (Kulite XT-190) at measuring points in Fig.2. Sampling

frequency of pressure and number of samples are 500 kHz and 4096, respectively. Pressure oscillations in the vortex chamber was estimated by frequency analysis.

3. Experimental conditions

In the present study, the effect of the height of the rod h, the exit cross section ratio (the ratio of the discharge collector cross section to vortex chamber outlet cross section) A_{exit}/A_{out} and diameter of chamber exit d_{out} on the temperature separation were investigated experimentally. Further, the effects of position and configuration of cavity (D_c) on the temperature separation were also shown quantitatively. Figure 3 shows details of four positions (P1, P2, P3, P4). Experimental conditions are shown in Table 1 for P1 and in Table 2 (d_c/D_c=0.25) for P2, P3 and P4, respectively.

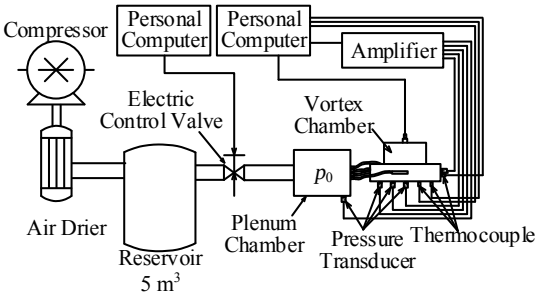

Fig. 1 Experimental apparatus

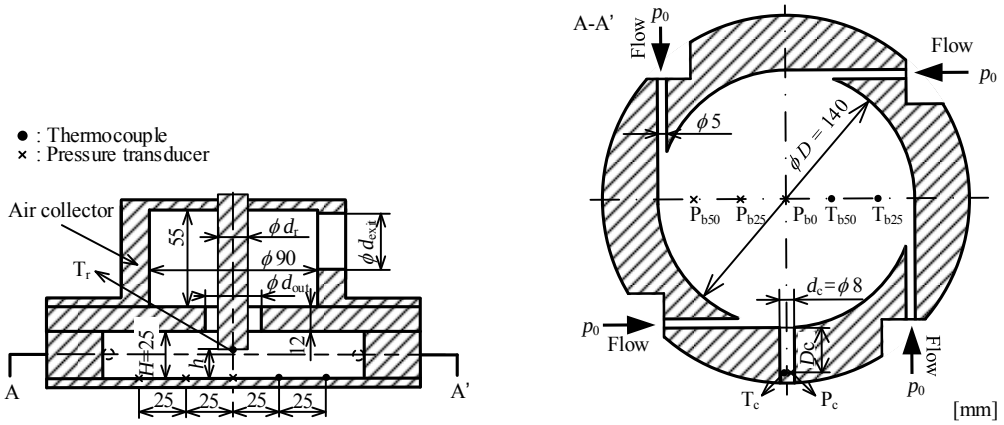

(a) Cross-section front view (b) Cross-section top view

Fig. 2 Schematic of vortex chamber

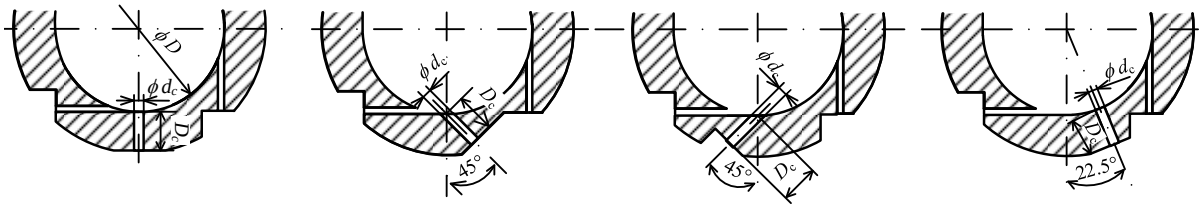

(a) P1 (b) P2 (c) P3 (d) P4

Fig. 3 Position of cavity (d_c = 8 mm)

Table 1 Experimental conditions for cavity position P1

$A_{out} = \pi(d_{out}^2 - d_r^2)/4$, $A_{exit} = \pi d_{exit}^2/4$

Case	d_{out}/D	A_{out} (mm^2)	A_{exit} (mm^2)		A_{exit}/A_{out}	h/H	d_c/D_c
P1-01	0.18	36π (d_{out}=20 mm)	7.3π	(d_{exit}=5.4 mm)	0.2	0.2	0.25
P1-02			25π	(d_{exit}=10.0 mm)	0.7	0.2	0.25
P1-03			43.6π	(d_{exit}=13.2 mm)	1.2	0.2	0.25
P1-04	0.21	161π (d_{out}=30 mm)	32π	(d_{exit}=11.3 mm)	0.2	0.2	0.25
P1-05			112.4π	(d_{exit}=21.2 mm)	0.7	0.2	0.25
P1-06			193.2π	(d_{exit}=27.8 mm)	1.2	0.1	0.25
P1-07							2.0
P1-08							1.0
P1-09						0.2	0.5
P1-10							0.25
P1-11						0.4	0.25
P1-12	0.29	336π (d_{out}=40 mm)	67.2π	(d_{exit}=16.4 mm)	0.2	0.2	0.25
P1-13			235.6π	(d_{exit}=30.7 mm)	0.7	0.2	0.25
P1-14			400π	(d_{exit}=40.0 mm)	1.2	0.2	0.25

Table 2 Experimental conditions cavity position P2, P3 and P4 (d_c/D_c = 0.25)

$A_{out} = \pi(d_{out}^2 - d_r^2)/4$, $A_{exit} = \pi d_{exit}^2/4$

Case	d_{out}/D	A_{out} (mm^2)	A_{exit} (mm^2)	A_{exit}/A_{out}
P2-01 P3-01 P4-01	0.14	36π (d_{out}=20 mm)	43.6π (d_{exit}=13.2 mm)	1.2
P2-02 P3-02 P4-02	0.21	161π (d_{out}=30 mm)	32π (d_{exit}=11.3 mm)	0.2
P2-03 P3-03 P4-03			112.4π (d_{exit}=21.2 mm)	0.7
P2-04 P3-04 P4-04			193.2π (d_{exit}=27.8 mm)	1.2
P2-05 P3-05 P4-05	0.29	336π (d_{out}=40 mm)	400π (d_{exit}=40.0 mm)	1.2

4. Result and discussions

Figure 4 shows the relationship between the change of static temperature $(T-T_a)/T_a$ and pressure ratio p_0/p_a for P1 (d_c/D_c=0.25). In each figure, the effects of A_{exit}/A_{out} (Fig.4a), d_{out}/D (Fig.4b) and h/H (Fig.4c) on temperature separation are shown at the positions of T_c, T_r, T_{b50} and T_{b25}.

In Figs.4(a) and 4(b), temperature separation (temperature difference between T_r and T_c) becomes the largest in cases of $A_{exit}/A_{out,}$ = 1.2 and d_{out}/D = 0.21. In Fig.4(c), temperature increases with an increase of h/H with the exception of h/H=0.4 and it is found that there is no effect of h/H on the temperature at Tc compared with the results of Figs.4(a) and 4(b). As a result, configuration of d_{out}/D = 0.21, $A_{exit}/A_{out,}$ = 1.2, h/H=0.2 is the most suitable to obtain a large temperature separation for P1

Figure 5(a) shows the time histories of static pressure and temperature at the bottom of the cavity at d_{out}/D=0.21, A_{exit}/A_{out}=1.2 and h/H=0.2. Both of the axes indicate static pressure and the temperature difference which are nondimensionalized by stagnation pressure p_o and temperature T_a, respectively. From this figure, the increase of

temperature is observed during Δt_3 - Δt_5, and not observed in Δt_1 and Δt_2. Further, amplitude of the pressure oscillation becomes large when the temperature increase is observed. In addition, the oscillation has the same dominant frequency of 3 kHz in each Δt. This result was also obtained at the other measuring points except for P_{b0}. Characteristics of pressure oscillation in the cavity depend on the behavior of shear layer generated from the leading edge of the cavity. As a result, it is considered that periodical oscillation with large amplitude from t =150 seconds is due to strong interaction of the trailing edge of the cavity with the shear layer.

Figure 5(b) shows the time histories of static temperature and pressure at the bottom of the cavity at d_{out}/D=0.21, A_{exit}/A_{out}=0.2 and h/H=0.2. In the case without the increase of temperature, the dominant frequency as shown in Fig.5(a) is not observed at each measuring point. In the present experimental conditions, the increase of temperature was observed in case of dominant frequency of 3 kHz. As a result, it is considered that the temperature increase in the cavity is associated with the oscillation of the pressure generated due to the behaviour of shear layer at the leading edge of the cavity.

Figure 6 shows the relationship between the change of static temperature $(T\text{-}T_a)/T_a$ and pressure ratio p_0/p_a in cases of d_c/D_c = 0.25, 0.5, 1.0 and 2.0 for P1 (d_{out}/D=0.21, A_{exit}/A_{out}=1.2, h/H=0.2). As seen from this figure, there is a large increase of temperature at $d_c/D_c \leq 1.0$ and the increase of temperature is small at $d_c/D_c > 2.0$. However, the decrease of temperature (T_r) does not depend on d_c/D_c.

In Fig.7, the effect of the cavity position (P1, P2, P3, P4) on temperature separation is shown for d_{out}/D=0.21, A_{exit}/A_{out}=1.2, h/H=0.2 and d_c/D_c=0.25. It is found from this figure that there is a large temperature separation at the positions of P3 and P4 and it is particularly the largest for P4 except for P_1. From Figs. 6 and 7, static temperature at T_r does not depend on the position and configuration of cavity and it is strongly affected by d_{out}/D and A_{exit}/A_{out}. It is considered that a cause of the temperature increase in the cavity is different from the cause of the temperature decrease in the center of the vortex chamber (T_r).

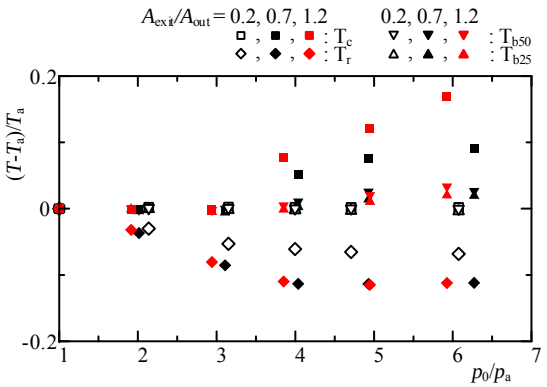

(a) A_{exit}/A_{out} = 0.2, 0.7 and 1.2 (d_{out}/D = 0.21, h/H = 0.2)

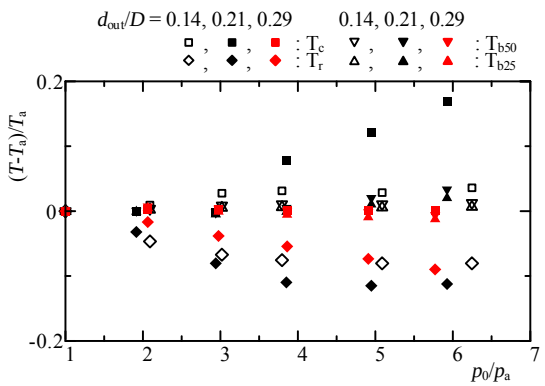

(b) d_{out}/D = 0.14, 0.21 and 0.29 (A_{exit}/A_{out} = 1.2, h/H = 0.2)

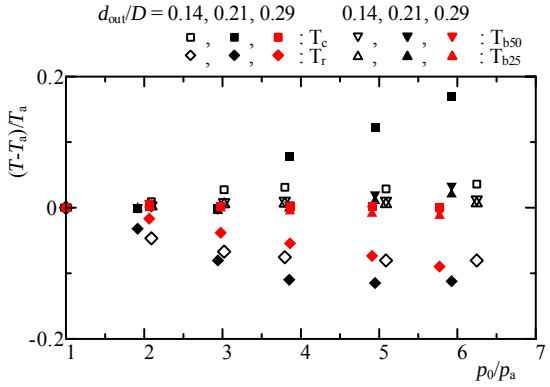

(c) h/H = 0.1, 0.2 and 0.4 (d_{out}/D = 0.21, A_{exit}/A_{out} = 1.2)

Fig. 4 Relationship between $(T\text{-}T_a)/T_a$ and p_0/p_a (P1, d_c/D_c = 0.25)

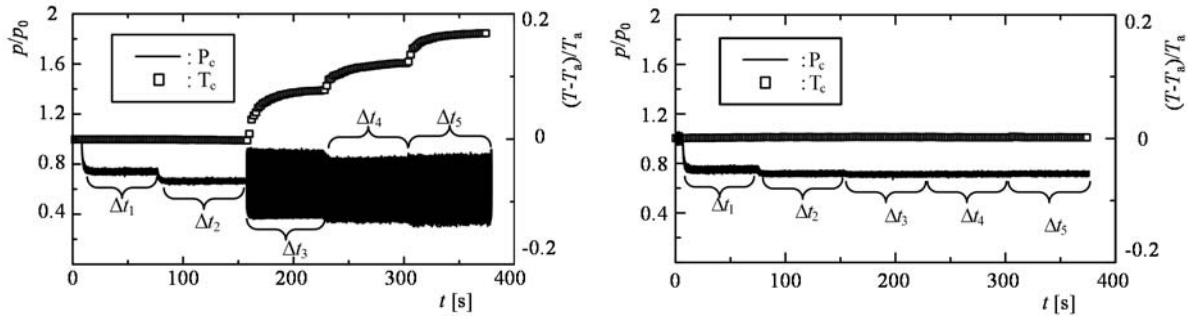

(a) A_{exit}/A_{out} = 1.2 (b) A_{exit}/A_{out} = 0.2

Fig.5 Pressure and temperature time histories (P1, d_{out}/D = 0.21, h/H = 0.2, d_c/D_c = 0.25)

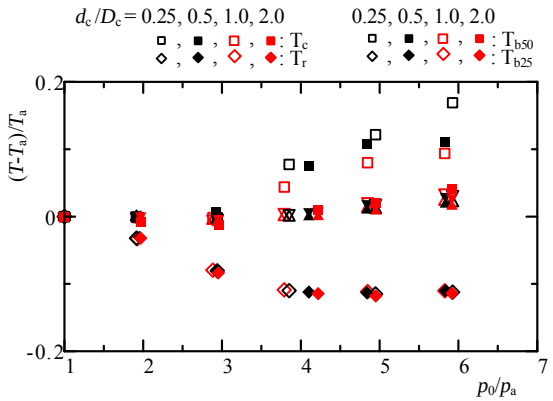

Fig. 6 Relationship between (T-T_a)/ T_a and p_0/p_a for d_c/D_c = 0.25, 0.5, 1.0 and 2.0 (P1, d_{out}/D = 0.21, A_{exit}/A_{out} = 1.2, h/H = 0.2)

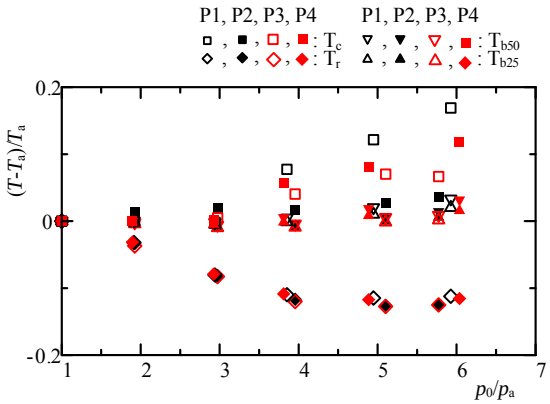

Fig. 7 Relationship between (T-T_a)/ T_a and p_0/p_a for P1, P2, P3 and P4 (d_{out}/D = 0.21, A_{exit}/A_{out} = 1.2, h/H = 0.2, d_c/D_c=0.25)

Figure 8(a) shows the relationship between the change of static temperature (T-T_a)/T_a and pressure ratio p_0/p_a in cases of A_{exit}/A_{out}=0.2, 0.7 and 1.2 (P4, d_c/D_c=0.25, d_{out} /D=0.21, h/H=0.2). From this figure, the largest temperature increase and temperature decrease in the center of the vortex chamber (T_r) is observed for A_{exit}/A_{out}=1.2. In Fig.8(b), the relationship between the change of static temperature (T-T_a)/T_a and pressure ratio p_0/p_a is shown in cases of d_{out} /D=0.14, 0.21 and 0.29 (P4, d_c/D_c=0.25, A_{exit}/A_{out}=1.2, h/H=0.2). The increase of temperature is small for d_{out}/D=0.14, 0.29 and temperature decrease in the center of the vortex chamber (T_r) is the largest. Further, it is found that the effect of d_{out}/D and A_{exit}/A_{out} on temperature separation in Fig.8 is almost similar to that in Fig.4 qualitatively.

Figure 9(a) shows the time histories of static pressure p/p_0 and temperature (T-T_a)/T_a at the bottom of the cavity at d_c/D_c=0.25, d_{out}/D=0.21, A_{exit}/A_{out}=1.2, h/H=0.2 (P4). From this figure, the increase of temperature is observed during Δt_3 - Δt_5, and not observed in Δt_1 and Δt_2. It is found from this figure that amplitude of the pressure oscillation becomes large when the temperature increase is observed in the same manner as the result in Fig.5. However, temperature increase and amplitude of pressure are small in comparison with results of Fig.5(a). In addition, the oscillation has the same dominant frequency of 3 kHz in each Δt. This result was also obtained at the other measuring points except for P_{b0}.

In general, it is known that the dominant frequency of the pressure fluctuation in the cavity depends on the velocity upstream of the cavity and configuration of the cavity. However, the cause of the pressure oscillation with the dominant frequency of 3 kHz in Figs.5(a) and 9(a) is not clear at the present time and it is found that the dominant frequency does not depend on the cavity position from Figs.5(a) and 9(a).

In Fig.9(b), the time histories of static temperature and pressure at the bottom of the cavity are shown for d_c/D_c=0.25, d_{out}/D=0.21, A_{exit}/A_{out}=0.2, h/H=0.2 (P4). In the case without the increase of temperature, the dominant frequency as shown in Fig.5(a) is not observed at each measuring point. In the present experimental conditions, the increase of temperature was observed in case of dominant frequency of 3 kHz. As described in Fig.5, it is considered that the temperature increase in the cavity is associated with the oscillation of the pressure.

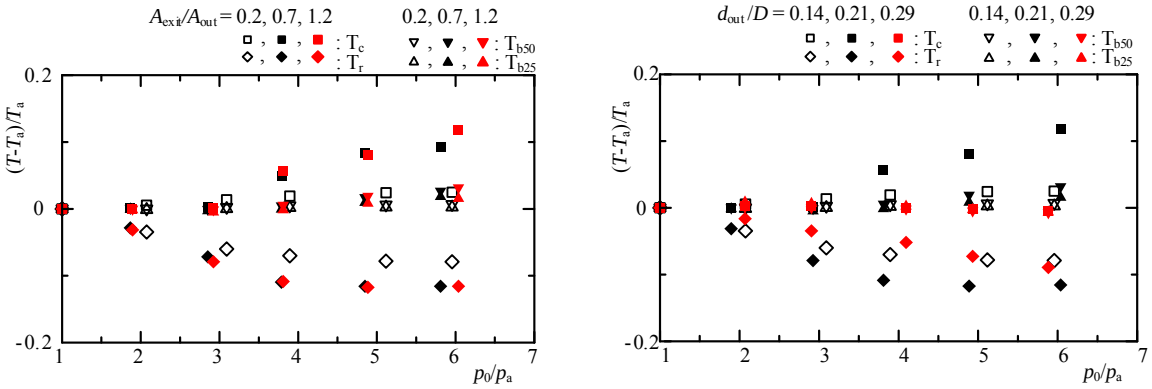

(a) A_{exit}/A_{out}=0.2, 0.7 and 1.2 (d_{out}/D = 0.21) (b) d_{out}/D = 0.14, 0.21 and 0.29 (A_{exit}/A_{out} = 1.2)

Fig.8 Relationship between (T-T_a)/ T_a and p_0/p_a (P4, h/H = 0.2, d_c/D_c = 0.25)

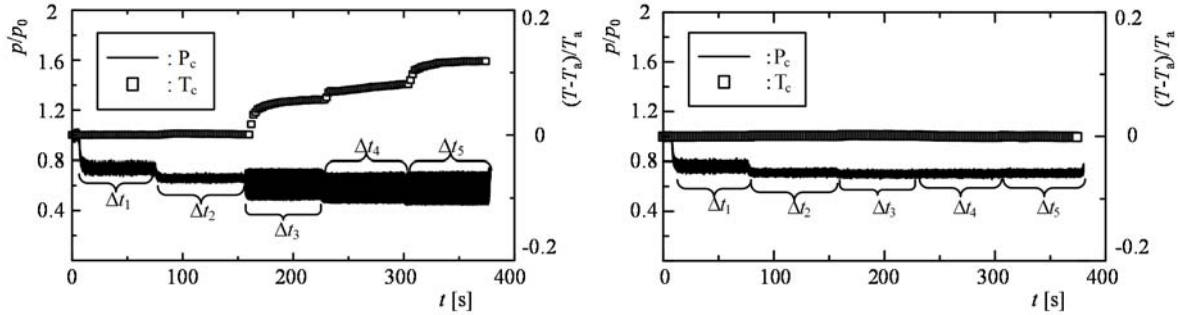

(a) A_{exit}/A_{out} = 1.2 (b) A_{exit}/A_{out} = 0.2

Fig.9 Pressure and temperature time histories (P4, d_{out}/D = 0.21, h/H = 0.2, d_c/D_c = 0.25)

5. Conclusions

An experimental study has been made to investigate the effects of configuration of vortex chamber including a cavity and cavity position on temperature separation in the vortex chamber were investigated experimentally. Further, the cause of temperature increase and flow behavior in the vortex chamber was investigated by numerical simulation. The results obtained are summarized as follows :

(1) The increase of temperature in the cavity was dependent on A_{exit}/A_{out}, d_{out}/D and h/H. On the other hand, the decrease of chamber central zone was dependent on A_{exit}/A_{out} and d_{out}/D.
(2) In case of the occurrence of temperature increase, pressure oscillations with a large amplitude was observed.
(3) The temperature increase in the cavity may be associated with the oscillation of the pressure generated due to the behaviour of shear layer at the leading edge of the cavity.
(4) Temperature change for P4 showed a similar tendency to that for P1 qualitatively and the decrease of temperature did not depend on the depth of cavity.
(5) The decrease of temperature in the chamber central zone was not dependent on the cavity configuration.

References

[1] M. Kurosaki, Acoustic streaming in swirling flow and the Ranque-Hilsch (vortex-tube) effect, J. Fluid Mech. 124 (1982), pp. 139-172.
[2] X. Yunpeng, A. Maziar, K. Richard, Critical review of temperature separation in a vortex tube, Experimental Thermal and Fluid Science 34 (2010), pp. 1367-1374.

[3] S. Eiamsa, P. Promvonge, Review of Ranque–Hilsch effects in vortex tubes, Renewable and Sustainable Energy Reviews 12 (2008), pp. 1822-1842.
[4] Y. Beliavsky, Experimental investigation of a temperature separation effect inside a short vortex chamber, Proceedings of the 9th International Conference on Heat Transfer, Fluid Mechanics and Thermodynamics, 2012, pp. 1482-1487.
[5] Y. Beliavsky, The Pressure Gradient Elastic Wave: Energy Transfer Process for Compressible Fluids with Pressure Gradient, Journal of Mechanics Engineering and Automation 3(2013), pp. 53-64.
[6] S. Anish, T. Setoguchi, H.D. Kim, Computational Investigation of the Energy Separation in Vortex Chamber, Proceedings of the Institution of Mechanical Engineers, Part C, Journal of Mechanical Engineering Science, February, 2013, pp. 1-29.
[7] K. Yokoo, S. Matsuo, Y. Matsuno, T. Setoguchi, H.D. Kim, Flow Characteristic in a Vortex Chamber, The Japan Society of Mechanical Engineers Kyushu Brunch, Kitakyushu, Paper No.620, (in Japanese), 2014.

Available online at www.sciencedirect.com

ScienceDirect

Procedia Engineering00 (2015) 000–000

Procedia Engineering

www.elsevier.com/locate/procedia

6th BSME International Conference on Thermal Engineering (ICTE 2014)

Numerical Simulation of Heat Transfer Coefficient on Turbine Blade using Intermittency Factor Equation

Most. Nasrin Akhter[a,*], Mohammad Ali [b], Ken-ichi Funazaki [c]

[a]*Department of Mathematics, Dhaka University of Engineering and Technology, Gazipur-1700, Bangladesh*

[b]*Department of Mechanical Engineering, Bangladesh Unversity of Engineering and Technology, Dhaka-1000, Bangladesh*

[c]*Department of Mechanical Engineering, Iwate University, Morioka 020-8551, Iwate, Japan*

Abstract

This paper deals with the numerical simulation of fluid flow and heat transfer coefficient on a gas turbine blade. The mathematical model of flow is based on the Reynolds Averaged Navier-Stokes (RANS) equations completed with the formulation of transition model by using an intermittency transport equation. An intermittency based transition model, which is critical for invoking transition onset according to Abu-Ghannam and Shaw correlation, is implemented into the proven Reynolds-Averaged N-S (RANS) solver. The intermittent behavior of the transitional flow is incorporated into the computation by modifying the eddy viscosity μ_t, obtained from a turbulence model. Wilcox [4] low Reynolds $k-\omega$ turbulence model is employed to calculate the eddy viscosity and others turbulent quantities. This model is designated for the prediction of flow transition under the influence of freestream turbulence (FST). The current model is applied to prediction of a modern high pressure turbine experiment, and detail comparisons of the computational results with the experimental data are presented. The model has been shown to be capable of predicting the high pressure turbine flow transition under a variety of Reynolds number and free stream turbulence conditions.

Peer-review under responsibility of organizing committee of the 6th BSMEInternational Conference on Thermal Engineering (ICTE 2014).

Keywords: Boundary Layer; Bypass Transition; Turbulence model; Numerical Prediction; Intermittency Factor; Heat transfer; Turbine blade; Eddy viscosity; Freestream turbulence.

* Corresponding author. Tel.: +88-01749288044;
E-mail address: nasrin6092002@yahoo.com

Peer-review under responsibility of organizing committee of the 6th BSME International Conference on Thermal Engineering (ICTE 2014).

1. Introduction

Accurate predictions of the transition and heat transfer distributions that are strongly affected by the transition point on the boundary layer are crucial to the design of various kinds of turbomechinary. Since heat transfer and skin friction tends to increase dramatically throughout the transitional region, accurate prediction of this process is of practical importance in gas turbine industries. At this moment, unfortunately, the boundary layer transition is still a very difficult phenomenon to make a full understanding of and will stay as a long-lasting challenging problem. This is because the boundary layer transition is easily influenced by various kind of factors such as freestream turbulence, wake passing or surface roughness. It is widely accepted idea that the transition governed by the freestream turbulence or wake passing, which is called bypass transition, is a common mode of boundary layer transition in gas turbines. Therefore accurate prediction of bypass transition induced by freestream turbulence, which is called FST-induced bypass transition, is important but challenging task for developing reliable and highly efficient gas turbines.

In recent years, the applications of computational fluid dynamics (CFD) have widely spread over various engineering problems. As the turbulence modeling makes steady progresses over the years, FST-induced transition can be simulated to some extent nowadays, usually using RANS (Reynolds Averaged Navier-Stokes) based approach with low Reynolds version of two equation model. However such a prediction tended to predict too early transition onset and/or too fast completion of the transition in comparison of the measurements, even for the simple flat plate case. One of the successful approaches was proposed by Schmidt and Patankar [1] using Production Term Modification (PTM) method. In their method the production term of turbulent kinetic energy (TKE) for transitional boundary layer was described using an ordinary differential equation of first order that emulated the evolution process of the TKE as delayed first-order system. The approach of Schmidt and Patankar has failed to gain popularity even among the turbomachinery community probably because it requires two parameters in the differential equation to be determined empirically.

Sveningsson et al. [5] calculated the heat transfer coefficient on the turbine blades with v2-f model can predict the macroscopic flow field accurately. But it can’t make accurate prediction of transition point and heat transfer distributions.

An alternative approach for predicting the bypass transition, which is nowadays being implemented into some of the commercial codes, is the usage of intermittency. The concept of intermittency, a measure of the probability of a given point to be inside the turbulent region, has evolved from the need to distinguish between the uniform and random behaviors of the flow in the intermittent region. Recently Suzen and Huang [6] proposed sophisticated intermittency-based transition model by combining two intermittency equations (Stellant and Dick [2] and Cho and Chung [3] model). There transition model has turned out to be superior to the precedents in predicting the bypass transition , however some test cases identified that there still remained some discrepancies between the prediction and experimental data, in particular for high freestream turbulence cases (such as around 10%) that are commonly observed in the flow field of gas turbines (Simon, Qiu, & Yuan [14]). Their model also is not tested for predicting heat transfer coefficients so far. The present authors (N. Akhter & K.Funazaki [7]) introduced a new intermittency based transition model, using Schmidt and Patankar [1] boundary layer analysis code. Their model exhibited a comparable or in some cases better predicting capability than that of Suzen and Huang model.

N. Akhter & K. Funazaki [8], improved the intermittency transport equation due to introduce the boundary layer analysis code to the well-established highly accurate RANS code. The newly developed RANS code is tuned and tested against T3 series of experiments of Savill [9] and the prediction of flow field around the LP turbine airfoil that was extensively investigated by Simon et al. [14].

In the current research, we focus on the prediction of transitional flows in high pressure turbine applications by using recently developed transport model for intermittency of N. Akhter & K.Funazaki [8]. The main motivation in the development of this model is to predict flow transition under the influences of free stream turbulence and Reynolds number effects. To further demonstrate the ability of the current model in predicting transitional flows, we focus the calculations of the experiment of Kang et al. [16] and Radomsky et al. [17] on the turbine blade of

PW6000 engine developed by Pratt & Whitney. In both experiments the effect of free stream turbulence and Reynolds number on transitional boundary layer investigated. Secondly, the intermittency transport model is presented and implementation of the model is described along with the empirical correlations employed for the onset of transition and the numerical details of prediction process are given. In section 3, the predictions of intermittency model are compared against the experimental data. Conclusion is provided in last section as usual.

Nomenclature

p	Static pressure	St	Stanton number
q_w	Heat flux on the wall	T	Temperature
T_{in}	Temperature at inlet	Tu	Turbulence intensity
γ	Intermittency factor	θ	Momentum thickness
μ	Molecular viscosity	μ_t	Eddy viscosity

2. New Transition Model

RANS based intermittency transport equations (abbreviated as ITE) have been developed as shown in following by modifying Cho and Chung [3] model. The aim of this modification is to improve the capability of the original model for predicting transition of wall bounded shear flows and at the same time reproduces the intermittency profile in the cross stream direction. The model is designated for the predict on flow transition under the influence of free stream turbulence and pressure gradients. The proposed transport equation is coupled with Wilcox [4] low Reynolds $k-\omega$ model with no modification.

2.1 Intermittency (γ) equation

The proposed intermittency equation is

$$\frac{\partial}{\partial x_j}(\rho u_j \gamma) = c_{g_1}\gamma(1-\gamma)\frac{P_k}{k} + \frac{cg2}{\beta^*}\rho\frac{k}{\omega}\frac{\partial\gamma}{\partial x_j}\frac{\partial\gamma}{\partial x_j} + \frac{\partial}{\partial x_j}\left[\sigma_\gamma(1-\gamma)(\mu+\mu_t)\frac{\partial\gamma}{\partial x_j}\right] \tag{1}$$

The first term of right hand side represents the production term, where $P_k = 2\mu_t' S^2$ represents the production of turbulent kinetic energy by the shear stress, where $\mu_t' = \frac{k}{\omega}$. This term expresses the generation of γ owing to the production of the turbulent kinetic energy. The second term represents the increase of γ by the spatial inhomogeneity or gradient of γ itself. The last term represents the diffusion term. The role of diffusion term is to allow a gradual variation of γ towards zero in the free stream.

Here presented intermittency transport equation is coupled with the turbulent kinetic energy *k* and its dissipation equation ω where, the original Cho and Chung [3] model was coupled with the turbulent kinetic energy and its dissipation rate ε. The conversion of ITE from $k-\varepsilon$ base to $k-\omega$ base was made simply using $\varepsilon = \beta^*\omega k$, where $\beta^* = 0.09$. Details will appear in the following.

The present model also differs from the original version of Cho and Chung [3] in diffusion term and empirical constants. The proposed new diffusion term is expected to induce gradual increase of intermittency in the streamwise direction with the newly selected set of model constants tuned for wall bounded shear flows. Note that the original model constants were selected based only on plane jet experiments. Since any sink term dose not exists in the original model of Cho and Chung, the destruction effect is embodied by decreasing the model constant C_{g1}, which controls overall transitional behaviour. In the present model the value of C_{g1} was set to be 0.19 based on the previous finding by the authors [7], where the original constant was 1.6. The model constant C_{g2}, which is appeared in second source term is set to be 1.0 instead of original constant 0.15. As shown, this constant affects the transition lengths in higher turbulence intensity cases, and its value was finally determined through numerical experiments N. Akhter [18] so as to achieve reasonable agreement with the measured data for the wide range of turbulence intensity.

We have dropped the entrainment effect as this effect is found to be negligible for most flows.

The intermittency concept was incorporated in to the computation through the eddy viscosity. The eddy viscosity relation then modifies

$$\nu^*_t = \nu_t\left[1 + C_{\mu g}\frac{k}{\omega^2}\gamma^{-2}(1-\gamma)\frac{\partial\gamma}{\partial x_k}\frac{\partial\gamma}{\partial x_k}\right] \tag{2}$$

The above expression for the eddy viscosity was originally proposed by Cho and Chung [3] to account for the effect of outer irrotational fluid motion. The above relation Eq.(2) reduces to the fully turbulent flow, when $\gamma = 1.0$. Eddy viscosity ν_t is calculated from the Wilcox low Reynolds $k-\omega$ model in the present model. Finally the model empirical constants adopted are

$$c_{\mu g} = 0.001 \quad c_{g1} = 0.19 \quad c_{g2} = 1.0 \quad \sigma_\gamma = 1.0 \tag{3}$$

2.2 Baseline turbulence model and onset location

As mentioned above, the two equation $k-\omega$ turbulence model of Wilcox [4] was chosen. The $k-\omega$ model is the model of choice in the sublayer of the boundary layer. Unlike any other model, the $k-\omega$ model does not involve damping functions and, of its simplicity, the $k-\omega$ model is superior to other models. Furthermore, it is as accurate as any other model in predicting the mean flow profiles. The model reads as follows,

Turbulent Kinetic energy (k)

$$\frac{\partial}{\partial t}(\rho k) + \frac{\partial}{\partial x_j}(\rho u_j k) = \tau_{ij}\frac{\partial u_i}{\partial x_j} - \beta^*\rho\omega k + \frac{\partial}{\partial x_j}\left[(\mu + \sigma^*\mu_T)\frac{\partial k}{\partial x_j}\right] \tag{4}$$

Dissipation rate of turbulent kinetic energy (ω)

$$\frac{\partial}{\partial t}(\rho\omega) + \frac{\partial}{\partial x_j}(\rho u_j \omega) = \alpha\frac{\omega}{k}\tau_{ij}\frac{\partial u_i}{\partial x_j} - \beta\rho\omega^2 + \frac{\partial}{\partial x_j}\left[(\mu + \sigma\mu_T)\frac{\partial\omega}{\partial x_j}\right] \tag{5}$$

And eddy viscosity,

$$\nu_t = \alpha^*\frac{k}{\omega} \quad \text{where} \quad \alpha^* = \frac{\alpha_0^* + \mathrm{Re}_t/R_k}{1 + \mathrm{Re}_t/R_k}, \quad \alpha = \frac{5}{9}\frac{\alpha_0 + \mathrm{Re}_t/R_\omega}{1 + \mathrm{Re}_t/R_\omega}(\alpha^*)^{-1}, \quad \beta^* = \frac{9}{100}\frac{5/18 + (\mathrm{Re}_t/R_\beta)^4}{1 + (\mathrm{Re}_t/R_\beta)^4} \tag{6}$$

The empirical constants of the Wilcox model are

$$\beta = \frac{3}{40}, \quad \sigma^* = \sigma = 0.5, \quad \alpha_0^* = \frac{\beta}{3}, \quad \alpha_0 = 0.1, \; R_k = 6, \quad R_\omega = 2.7, \quad R_\beta = 8 \tag{7}$$

One of the important points associated with transition prediction using the intermittency-based turbulence model is to specify the transition onset point properly since the intermittency transport equation does not feature a capability to tell where the transition will occur. This study has employed the well known Abu-Ghannam and Shaw [10] correlation for determining onset location, which is given as follows;

$$\mathrm{Re}_{\theta_t} = 163 + \exp(6.91 - Tu) \tag{8}$$

where Tu is turbulence intensity at a reference point and Re_{θ_t} is the Reynolds number based on momentum thickness at onset location. Before the onset location, the production term of turbulent kinetic energy was set to be zero inside the boundary layer.

2.3 Numerical Method

Calculations have been done by the CFD code developed by Yamada et al. [15]. The three dimensional Reynolds averaged Navier-Stokes equations are discretized spatially by a cell-centered finite volume formulation and in time

using the Euler implicit method. The inviscid fluxes at cell interfaces are evaluated using a highly accurate upwind scheme based on a TVD formulation (Furukawa et al. [13]), where a Roe's approximate Riemann solver of Chakravarthy [12] and third order accurate MUSCL- type approach of Anderson et al. [11] with the Van Albada limiter were implemented. The viscous fluxes are determined in a central differencing manner with Gauss's theorem. Simultaneous equations linearized in time were solved by a point Gauss-Seidal relaxation method. To obtain a time accurate solution, inner iteration so called Newton iteration, is introduced at each time step. The code is able to deal with the multi-blocked computational grid system taking advantage of MPI.

2.4 Computational domain

The target of our research is the Turbine blade of PW6000 engine, a jet engine developed by Pratt & Whitney. It is regarded as the benchmark in the studies of the prediction of heat transfer coefficient. The experiment chosen for validating the computations carried out in this work is the measurement of Radomsky et al. [17] for heat transfer coefficient and Kang et al. [16] for pressure coefficient on the turbine blade with free stream turbulence. We use these results to check the accuracy of our predictions. The detailed geometric parameter of the vane and the experimental parameter are listed in Table1.

In these experiments, a stator vane was scaled up by a factor of nine and placed in a large scaled wind tunnel. The stator vane geometry was a two dimensional slice of an engine profile taken at the vane midspan. The experiments consisted of a linear cascade of three vanes, and it was approximated as the turbine cascade. The central vane constructed by stacking rigid polystyrene pieces 5 cm thick and on the outside of the central vane surface, 50 mm thick type 304 stainless steel foils were attached to the polystyrene. The metal foil provided a constant heat flux boundary condition on the blade surface. The details of this experiment have been documented by Radomsky et al. [17] and Kang et al. [16].

The computational mesh was created using the Gridgen Pre-processor. This mesh generator is well suited for creating grids as the domain can be split into several sub domains in a top-down approach allowing for good control of each sub domain of the mesh. When the mesh is completed the sub domains can be clustered in larger blocks for output.

In the simulations the computational domain is an eight block domain. It consists of an O-grid around the stator vane, ensuring high quality cells in the important near wall region; In the cross stream direction with the first wall unit grid spacing y^+ approximately equal to 0.5. The grid dependency study was first performed in a linear cascade and the sensitivity was checked. Fig.1 shows the comparisons of pressure co-efficient profiles for $\mathrm{Re}_{ex} = 1.2\times10^6$ along the airfoil surface using surface grid points 200 and 300 along streamwise direction. It can be seen that the pressure coefficient distributions given by two grid are essentially same and both agree with the experiment fairly well. All results are reported here by the use of total grid points 233200. Where the surface grid number was 200 along streamwise direction and 100 grid points along cross stream direction. Inlet of the domain is located one chord length upstream of the stator vane stagnation point. This distance has been used by investigators (Radomsky & Thole, [17]) and has proved to be sufficient. The no-slip and constant heat flux condition is imposed on the wall boundary, informed as suction side and pressure side in Fig. 2. In span direction and pitch direction, periodic condition is imposed.

Table1:Geometry and flow conditions for the stator vane.

Scaling factor	9
Scaled-up chord length(C)	59.4cm
Pitch/Chord (P/C)	0.77
Span/Chord(S/C	0.93
Re_{in}	2.3×10^5
Inlet and exit angles	0^0 and 78^0

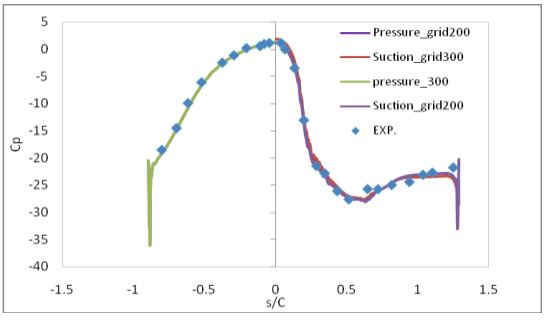

Fig.1 Grid sensitivity study

Inlet condition has uniform velocity with free stream turbulence and uniform thermal distribution. In Table 1, the calculation parameters are presented. In this calculation all variables are normalized. The normalized temperature is defined as the following equation

$$T^* = \frac{T - T_0}{T_{in} - T_0} \tag{9}$$

In Fig. 2(a) the computational domain where every 5th grid line have shown and Fig.2 (b) shows some regions of the grid in detail.

3. Results and Discussion

The current transition model was applied to predict the heat transfer on the turbine blade PW6000. The experiment chosen for the computations carried out in this work is the measurements of Kang et al. [16] and Radomsky et al. [17]. They provide a detailed set of both flow field and heat transfer measurements including documented inlet profiles, a combination rarely found in the literature. Results for the two Reynolds numbers investigated in this study are presented for pressure coefficient and two free Stream turbulence intensity (FSTI) investigated for Stanton number. The present approach is validated against the experiments to address the issue of Reynolds number and free stream turbulence effect.

3.1 Calculation of Static pressure

In this study two Reynolds number $\mathrm{Re}_{ex} = 6\times10^5$ and $\mathrm{Re}_{ex} = 1.2\times10^6$ have been studied. In both cases exit Reynolds number is used and free stream turbulence intensity was set as 1%. The pressure coefficient results for $\mathrm{Re}_{ex} = 6\times10^5$ and $\mathrm{Re}_{ex} = 1.2\times10^6$ are shown in Fig. 3(a) and 3(b) respectively. The pressure coefficient is defined by the equation

$$C_p = \frac{(P - P_{in})}{0.5\rho U_{in}^2} \tag{10}$$

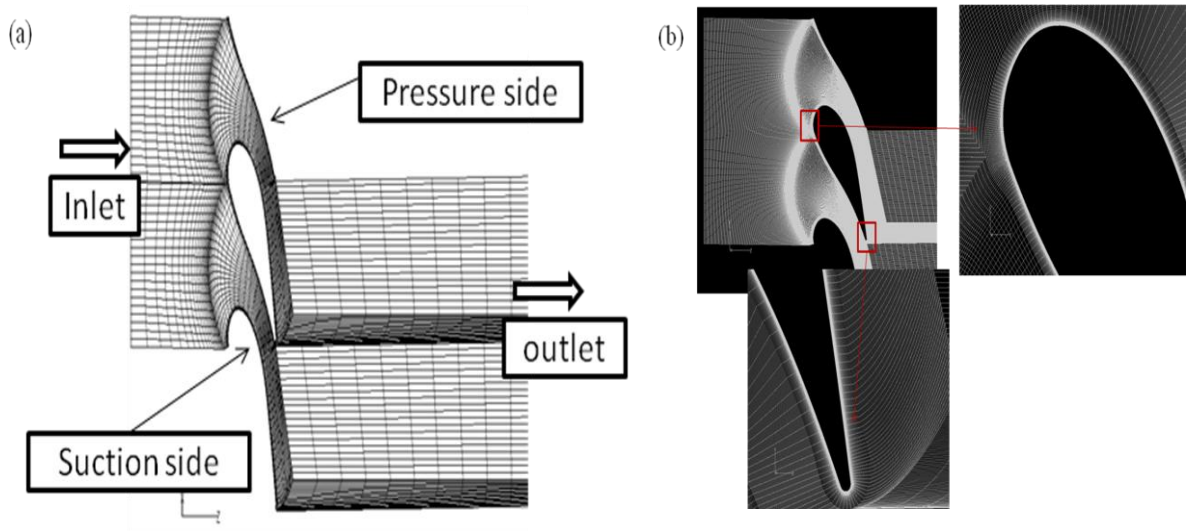

Fig. 2: a) Computational domain (every fifth line have shown) b) Close view of leading and trailing edge.

The results have been presented as normalized distance along the vane surface, with the pressure side on the left and the suction side on the right. The experimental data measured by Kang [16]. The strong acceleration on the suction side of the vane is clear from the rapidly decreasing value of c_p through $s/C = 0.3$. The flow continues to accelerate at a smaller rate unit $s/C = 0.5$ after which the velocity stays relatively constant with $c_p = -27$. Note that there are slightly lower values of c_p for high Reynolds number case, which have shown in Fig. 3(b). The flows slow down slightly beyond $s/C = 1$ near the trailing edge of the vane, flow on the pressure side of the vane accelerates monotonically. Good agreement is observed in both low and high Reynolds number case. The pressure coefficient contour for high Reynolds number have been shown in Fig. 3(c) and also compared with the measured data. The comparisons of contour for the high Reynolds number case show that there is a good agreement between the predicted and measured c_p values. The location and peak value of c_p agree quite well. The contour does not agree near the trailing edge of the vane because the flexible wall was not simulated in order to make domain periodic.

(a)

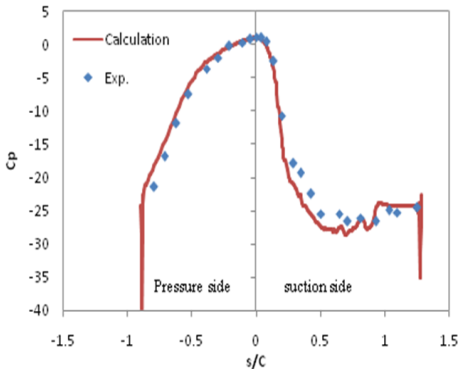

(b)

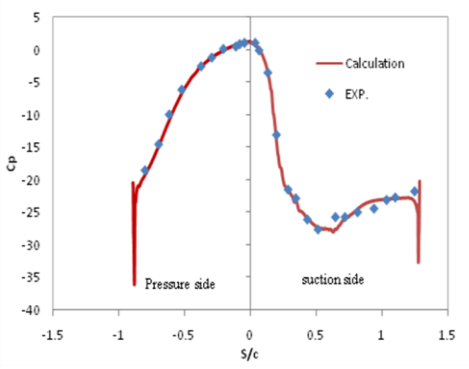

(c)

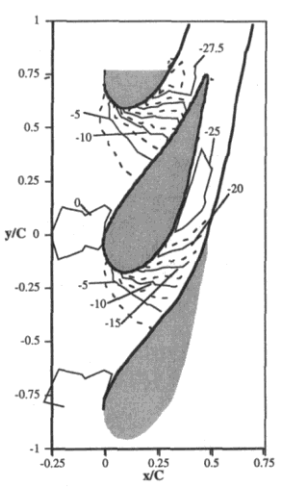

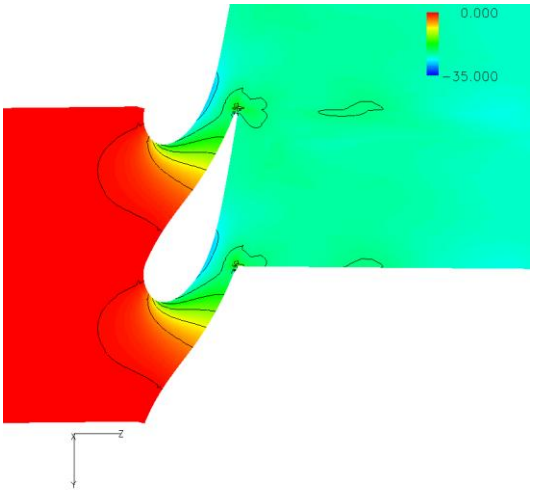

Pressure coefficient contour (Exp.) **Pressure coefficient contour (Simulation)**

Fig. 3: Comparisons of pressure coefficient between measurement and prediction a) for low Reynolds number b) for high Reynolds number c) comparison of contour for high Reynolds number.

3.2 Heat transfer calculation

The heat transfer results in terms of Stanton numbers based on the two free stream turbulence intensity 1% and 19.5% have been studied. For both cases the inlet Reynolds number have been taken $\mathrm{Re} = 6\times10^5$. In Fig. 4(a) and 4(b) show the comparison results of Stanton number in lower and higher Reynolds number respectively. The Stanton number calculated by the equation,

$$St = \frac{q_w}{\rho c(T_w - T_{in})U_{in}} \tag{11}$$

The results are compared with the experimental data of Radomsky [17]. It has been well documented that high free stream turbulence can greatly augment the surface heat transfer, Fig. 4(a) and 4(b) show the measured heat transfer along the vane surface for low and high free stream turbulence conditions respectively. For the low free stream turbulence conditions, the peak heat transfer occurs at $s/C = 0.25$, which is where the highest acceleration occurs along the shoulder of the suction side of the turbine vane and present calculation capture this region quite well. Also the comparable agreement is observed in onset location. For high free stream turbulence conditions, the Stanton numbers are relatively constant at elevated values, starting at the
stagnation location and extending to $s/C = 0.2$ followed by slight bump at $s/C = 0.25$. The transition location has moved significantly upstream on the vane surface for high free stream turbulence conditions relative to the baseline low free stream turbulence. Although on the pressure side of the vane ($s/C < 0$), in both cases the Stanton number is under estimated. From the comparisons it appears that the present model reasonably captured a general picture of the boundary layer transition on the blade suction side so that, the qualitatively prediction is achieved.

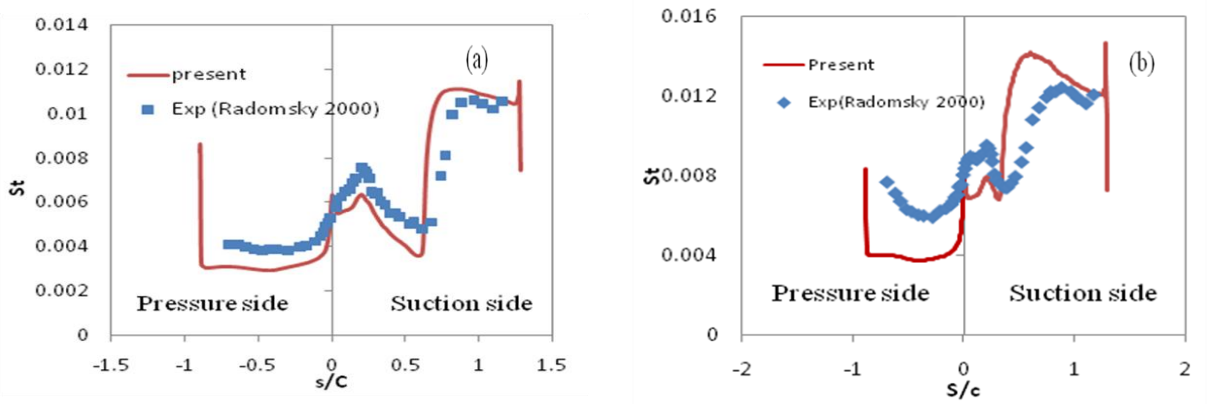

Fig. 4: Comparisons of Stanton number between the measurements and prediction

4. Concluding Remarks

A transition model, based on dynamic transport equation for the intermittency factor, has been presented with some improvements especially of prediction accuracy for high free stream turbulence case that are commonly found in gas turbines. An intermittency based new model was employed to predict heat transfer calculation on high pressure turbine. The new model was tested against transitional boundary layer of high pressure turbine PW6000 engine. The heat transfer calculation of high pressure
turbine cascade cases are generally believed to be difficult cases for any model in respect of onset point. Computations are performed two different Reynolds number and two different free stream turbulence intensity cases. Detailed comparisons with experiments are made for pressure coefficient and Stanton number. Overall, good agreement with the experimental data is obtained. Some discrepancies were observed between the prediction and the measurements. However, as whole, the approach seems promising and worthy of being implemented in the various types of RANS codes. This study demonstrated that the current intermittency based transition model is capable to

predict the pressure coefficient and the heat transfer co-efficient on a gas turbine blade over a range of Reynolds number and FSTI flow conditions. Further study is being continued to investigate the predicting capability of the current model in different kinds of flow fields.

References

[1] Schmidt, R. C., and Patanker, S. V., "Two-Equation Low-Reynolds –Number Turbulence Modeling of Transitional Boundary Layer Flows Characteristic of Gas turbine Blades," NASA Contractor Report 4145 (1988).

[2] Steelant, J., and Dick, E., "Modelling of bypass transition with conditioned NS equations coupled to an intermittency Transport Equation," Int. J. Numer. Methods Fluids, 23, (1996) pp. 193-220.

[3] Cho, J. R., and Chung, M. K., "A $k-\varepsilon-\gamma$ equation turbulence model," J. Fluid Mech., 237, (1992) pp. 301-322.

[4] Wilcox, D. C., "Simulation of Transition with Two Equation Turbulence Model" AIAA J., vol. 32, No. 2, (1994) pp. 247-255.

[5] Sevingson, A., Davidson. L., "Assessment of Realizability constraints in v^2-f turbulence models" J. Heat and Fluid Flow. 25, (2004), pp.785-794.

[6] Suzen, Y. B., and Huang, P. G., "Modelling of flow transition using an intermittency transport equation for modelling flow transition," J. Fluid Engg. Vol.122, (2000) pp.273-284.

[7] Akhter, M. N., Funazaki K., "Development of Prediction method of Boundary Layer Bypass transition using Intermittency factor Equation" International Journal of Gas Turbine, Propulsion and Power System, Vol.1 no.1.(2007) pp 30-37.

[8] Akhter, M. N., Funazaki, K., Yamada, K., "Numerical Simulation of Bypass transition by the Approach of Intermittency Transport Equation." Journal of Fluid Science and Technology, Vol. 4, No. 3, (2009) pp 524-535.

[9] Savill, A. M., "Some recent progress in the turbulence modeling of bypass transition," In: R.M.C. So, C.G. Speziale and B.E. Launder, Eds.: Near wall turbulent flows, Elsevier Science, (1993) pp. 829-848.

[10] Abu-Ghannam, B. J., and Shaw, R., "Natural transition of boundary layer the effect of turbulent pressure gradient and flow history," J. Mech. Engg.Sci. 22, no.5 (1980) pp. 213-228.

[11] Anderson, W. K., Thomas, J. L., and Van Leer, B., "Comparison of Finite Volume Flux Splitting for the Euler Equation," AIAA Journal, vol.24, No.9, (1986) pp. 1453-1460.

[12] Chakravarthy, S. R., "The Versatility and Reliability of Euler Solvers Based on High –Accuracy TVD Formulations" AIAA paper No. 86-0243 (1986).

[13] Furukawa, M., Yamasaki, M., and Inoue, M., "A Zonal approach for Navier-stokes Computations of Compressible Cascade Flow Fields Using a TVD Finite Volume Method," ASME Journal of Turbomechinary, Vol.113 No.4, (1991) pp. 573-582.

[14] Simon, T. W., Qiu, S., and Yuan, K., "Measurement in a Transitional Boundary Layer under Low-Pressure Turbine Airfoil Conditions" NASA CR 2000-209957, (2000).

[15] Yamada, K., Furukawa, M., Nakano, T., Inoue, M., Funazaki, K., "Unsteady Three-Dimensional Flow Phenomena Due to Breakdown of Tip Leakage Vortex in a Transonic Axial Compressor Rotor," ASME paper, GT 2004-53745. (2004)

[16] Kang, M. B., and Thole, K. A., "Flow field measurements in the end wall region of a stator vane," J. Turbomechinary vol. 122, (2000) pp. 458-466.

[17] Radomsky, R. W., and Thole, K. A., "Flow field measurements for a highly turbulent flow in a stator vane passage," J. Turbomechinary vol. 122, (2000) pp. 255-262.

[18] Akhter, M.N., "Development of Boundary Layer Bypass Transition Prediction Methods Based on Intermittency Factor," Doctoral Dissertation, Iwate University, (2008).

Available online at www.sciencedirect.com

ScienceDirect

Procedia Engineering 00 (2015) 000–000

Procedia Engineering

www.elsevier.com/locate/procedia

6th BSME International Conference on Thermal Engineering (ICTE 2014)

Design and Optimization of Compact Heat Exchangers to be Retrofitted into a Vehicle for Heat Recovery from a Diesel Engine

S Bari*, S N Hossain

Barbara Hardy Institute, School of Engineering, University of South Australia, Mawson Lakes Campus, SA 5095, Australia.

Abstract

Higher depletion rate and increasing price of fossil fuels have motivated many researchers to harness energy from the waste heat from internal combustion engines, and thus improve the overall efficiency. Among the waste heat recovery methods, the bottoming Rankine cycle is the most promising. In this technique, the recovered heat is used to produce additional power using turbine. In order to maximise the additional power production, an effective heat exchanger design is necessary. The main focus of the current research was to design heat exchangers which needed to be pancake-shaped to be retrofitted into a vehicle. The heat exchanges chosen were shell and U-tube type. CFD simulations were carried out to optimize the design of the heat exchangers and calculate the additional power that could be achievable by using this optimized pancake-shaped heat exchangers.

Peer-review under responsibility of organizing committee of the 6th BSME International Conference on Thermal Engineering (ICTE 2014).

Keywords: Engine, heat recovery, heat exchanger, CFD

1. Introduction

Diesel engines have a wide field of applications because of their higher efficiencies. Trucks, buses and earth moving machineries use high speed diesel engines. Diesel engines are also used in small electrical generating units or as standby units for medium capacity power stations. Engine based power production today represents around 10-15%

* Corresponding author. Tel.: +61 8 8302 3439; fax: +61 8 8302 3380.
E-mail address: Saiful.bari@unisa.edu.au

Peer-review under responsibility of organizing committee of the 6th BSME International Conference on Thermal Engineering (ICTE 2014).

Nomenclature

u,v,w	velocity component in x,y and z directions, respectively, m/s
T	temperature, K
ρ	density, kg/ m^3
τ	shear stress, N/m^2
γ	conductivity coefficient at bulk temperature of the fluid, W/mK

of the total installed capacity in the world [1]. Despite higher efficiency, a significant amount of input energy is expelled to the environment through the exhaust of a diesel engine. Hatazawa et al. [2] studied a water cooled diesel engine and found that about 25% and 40% of the input energy were wasted to the coolant and exhaust gases, respectively. So, generally, a typical diesel engine rejects 30-40% of the input energy through the exhaust gas of the engine. Since the wasted energy represents about two-thirds of the input energy [3], exhaust gas from diesel engines is a significant heat source which can be used in a number of ways to provide additional power and improve overall thermal efficiency of the engine. Therefore, WHR technologies as well as the use of alternative fuels will be able to reduce the harmful emissions per unit of power produced [4-7]. Exhaust gas has higher recovery potential than the coolant because of its higher temperature and greater exergy content [8].

Turbocharging [9, 10], cabin air-heating [11], desalination [12] and reducing engine warm-up time [13] are conventional technologies to utilize exhaust gas with a low recovery rate. Relatively new major technologies for WHR include turbocompounding and thermal WHR based on Rankine Cycle (RC), and Thermoelectric generation (TEG). Among these heat recovery systems, RC is the most promising. Hountalas et al. [14] developed a simulation model to describe the potential efficiency gain of a Rankine bottoming cycle applied to a HD truck powered by a diesel engine. They were able to improve the brake specific fuel consumption (bsfc) by 9%. Between the RC system and the turbo-compounding of WHR, Weerasinghe et al. [15] made a numerical simulation comparing their power output and fuel savings. The results revealed the relative advantages of the RC over turbo-compounding. According to their study, 7.8% of power was recovered by using the RC system whereas only 4.1% of power was recovered by using the turbocompounding. A similar comparison between different WHR systems was also conducted by Houtalas el al. in their study [16, 17]. They compared mechanical turbocompounding, electric turbocompounding, RC and organic Rankine cycle (ORC) based WHR by computer simulation to extract heat from the exhaust of a diesel engine. They found that mechanical turbocompounding, electric turbocompounding, and RC based WHR were capable of improving bsfc by 4.8%, 6.0%, and 9.0%, respectively.

With the exception of mechanical turbo-compounding, RC- and ORC-based heat recovery systems need to utilize heat exchangers to extract energy from the waste heat. The heat exchanger design is critical as it needs to provide an adequate surface area in order to cope with the thermal duty [18]. The pressure loss across the heat exchangers also needs to be reasonable to avoid back pressure that will have a negative impact on the net engine power and efficiency. These are the challenges needed to be investigated to design an effective heat exchanger to extract heat efficiently with a low pressure drop from the exhaust of the diesel engines. Another important challenge is to design a compact heat exchanger, if possible in pancake-shaped without sacrificing the performance to be retrofitted into vehicles.

This research aims to design a pancake-shaped shell and U-tube heat exchanger to be retrofitted in a sport utility vehicle (SUV). CFD simulations were carried out to calculate the additional power that could be achievable by using these heat exchangers.

2. Heat Exchanger Model

In order to construct and validate a model of heat exchanger, two heat exchangers were purchased from the market place and they were tested in a 4-stroke, 4-cylinders, water-cooled HINO W04D diesel generator-set. The gen-set was loaded with a 50 kVA resistive load. A photograph of the purchased heat exchanger is shown in Fig. 1. The existing heat exchanger model drawing was created by Computer Aided Design (CAD) software SolidWorks2012. In the model, 30° triangular staggered array layout was used for the tube arrangement of the heat exchanger. The geometry

model was then meshed using ANSYS meshing software. The ANSYS CFX14.0 was used to solve the equations for the fluid flow and heat transfer analysis.

Fig. 1: Purchased heat exchanger.

The modeling of the heat exchanger was based on steady state Navier-Stoke equations. The governing equations for the flow and conjugate heat transfer were modified according to the conditions of the simulation setup. As the problem was assumed to be steady, the time dependent parameters were dropped from the equations. The resulting equations are:

Continuity equation: $$\nabla \cdot \left(\rho \vec{V}\right) = 0 \tag{1}$$

Momentum equations:

x-momentum: $$\nabla \cdot \left(\rho u \vec{V}\right) = -\frac{\partial p}{\partial x} + \frac{\partial \tau_{xx}}{\partial x} + \frac{\partial \tau_{yx}}{\partial y} + \frac{\partial \tau_{zx}}{\partial z} \tag{2}$$

y-momentum: $$\nabla \cdot \left(\rho v \vec{V}\right) = -\frac{\partial p}{\partial y} + \frac{\partial \tau_{xy}}{\partial x} + \frac{\partial \tau_{yy}}{\partial y} + \frac{\partial \tau_{zy}}{\partial z} + \rho g \tag{3}$$

z-momentum: $$\nabla \cdot \left(\rho w \vec{V}\right) = -\frac{\partial p}{\partial z} + \frac{\partial \tau_{xz}}{\partial x} + \frac{\partial \tau_{yz}}{\partial y} + \frac{\partial \tau_{zz}}{\partial z} \tag{4}$$

Energy: $$\rho c_p \left(u\frac{\partial T}{\partial x} + v\frac{\partial T}{\partial y} + w\frac{\partial T}{\partial z} \right) = \lambda \left(\frac{\partial^2 T}{\partial x^2} + \frac{\partial^2 T}{\partial y^2} + \frac{\partial^2 T}{\partial z^2} \right) \tag{5}$$

To solve the problem, the k-ω based Shear-Stress-Transport (SST) turbulent model [19] was employed and an energy equation was included in the model. The k-ω based SST model accounts for the transport of the turbulent shear stress and gives highly accurate predictions regarding the onset and the amount of flow separation under adverse pressure gradients. It is actually an eddy-viscosity based model which combines both the k-ε and k-ω models. The use of the k-ω formulation in the inner parts of the boundary layer makes the model applicable down to the wall through the viscous sub-layer, hence the k-ω based SST model can be used for low Reynolds number turbulence model without any extra damping functions.

In order to make the simulation more accurate, different meshing schemes were used. The solid tubes were meshed using sweep mesh whereas the fluid volumes were meshed using tetragonal-hybrid elements. The final refined mesh was selected by comparing the simulation results of model with different mesh density and meshing schemes. The final model of the heat exchanger had 11,773,030 elements and grid independent solution was acquired.

3. Results and Discussion

3.1. Experimental Results

At first, experiments were conducted with the purchased heat exchangers to determine the performance of the heat exchangers and then, the additional power recoverable was estimated. To do these, as mentioned before two identical shell and tube heat exchangers (Fig. 1) were purchased and experiment was conducted. The experimental results and the simulation results are compared and it is presented in Fig. 2. It is clear from the figure that the effectiveness found from the experiment was approximately 10% lower than the CFD simulation results. This could be due to the presence of fouling sources in both hot and cold fluids in the experiments. The presence of soot and particles in the exhaust gas can increase resistance to the heat transfer inside the tubes and the untreated water in the shell of the heat exchangers can have a fouling effect on the shell side. This would decrease the shell side and tube side heat transfer coefficients [20] resulting in a lower effectiveness in the experiments. These effects were not considered in the CFD simulation. Lei et al. [21] reported an 8% discrepancy between CFD simulations and experimental results. As the discrepancy found in the current model and the literature was close enough, it can be concluded that the model was appropriately constructed and the experimental and simulation results were in adequate agreement.

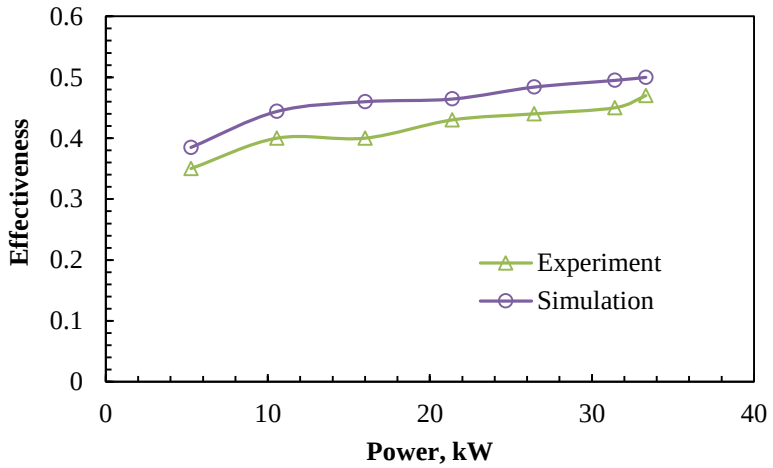

Fig. 2: Comparison of simulation results validation with experimental results.

From Fig. 2, the performance of the heat exchangers at different powers of the engine can be seen. The effectiveness was found to be 0.44 at the rated power of 26.43 kW. However, it is found from extensive literature review that the effectiveness of the shell and tube heat exchanger is reported to be in the range of 0.7 and 0.99 [22, 23]. Therefore, initially the performance of the design of the heat exchangers of round-shaped and then, pancake-shaped were optimized.

For round-shaped and pancake-shaped designs, the effects of important parameters of heat exchanger such as length, diameter of the shell, number and diameter of tubes on the performance of the heat exchangers were investigated. The potential additional power was then calculated using actual turbine efficiency [24, 25]. The round-shaped optimized heat exchanger was 2 m in length and the shell diameter was 90 mm. This heat exchanger could be used for diesel engine based stationary power generators as they do not have any space constraints. However, design of heat exchangers need to be compact and pancake-shaped to be retrofitted into a vehicle. So, attempts were made to redesign this round-shaped heat exchanger. During the redesign of the heat exchangers, the total heat transfer surface area of the round-shaped and the pancake-shaped heat exchangers were approximately kept constant. The shape of the heat exchanger was only changed to fit into a vehicle. The specifications of the optimized round-shaped and redesigned

pancake-shaped heat exchangers are presented in Table 1. The 3D model of the optimized round-shaped and redesigned pancake-shaped heat exchangers are presented in Fig. 3.

Table 1. Heat exchanger specification.

Features	Optimized heat exchanger	Redesigned heat exchanger
Shell	Outer diameter 96 mm	1100 × 160 × 90 mm
Tube No.	31	36
Tube diameter	OD 11mm, ID 9.44 mm	OD 13mm, ID 10 mm
Baffle design	50% cut, circular	50% cut, rectangular
Baffle No.	7	7

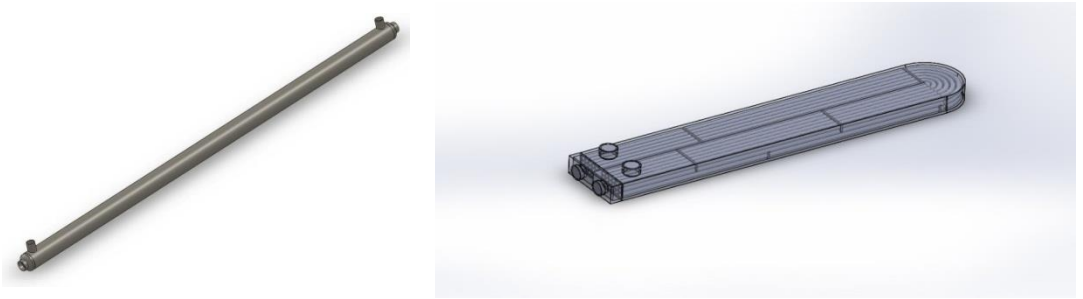

(a) (b)

Fig. 3. 3D model of heat exchanger (a) Optimized round-shaped (b) Optimized pancake-shaped.

3.2. Effectiveness of the heat exchanger

The comparison of the effectiveness of the optimized round-shaped and pancake-shaped heat exchangers is

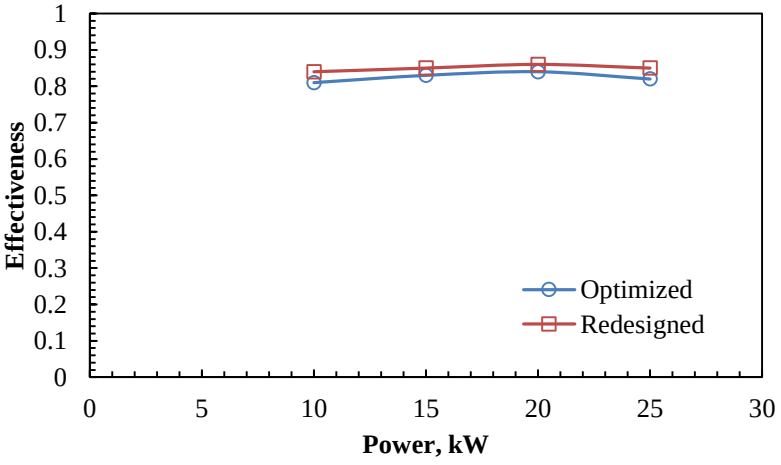

Fig. 4. Effectiveness variation at different power for round-shaped and pancake-shaped heat exchangers.

presented in Figure 4. It is evident from the figure that the effectiveness of pancake-shaped heat exchanger is on average 3% higher than that of the optimized round-shaped heat exchanger. Though it was intended to have equal surface area between round-shaped and pancake-shaped heat exchangers, but due to U-shape as can be seen in Fig. 3b, the total heat transfer area of the pancake-shaped heat exchanger was 5% higher than the round-shaped one. Also, as the fluid passed through the bend, it slowed down resulting more residence time for heat transfer. As a result, the effectiveness of the pancake-shaped heat exchanger was higher than the effectiveness of the round-shaped heat exchanger.

3.3. Additional power generation

Extra power that could be recoverable from the exhaust of the diesel engine with the proposed shell and tube heat exchangers is presented in Fig. 5. The additional power generation by extracting heat from the exhaust gas was calculated at different working pressures of the working fluid. It is found from the figure that the pancake-shaped heat exchanger was able to generate 7.1% higher additional power than the round-shaped one. The maximum additional powers achieved by optimized round-shaped and pancake-shaped heat exchangers were 9.8 kW and 10.5 kW, respectively.

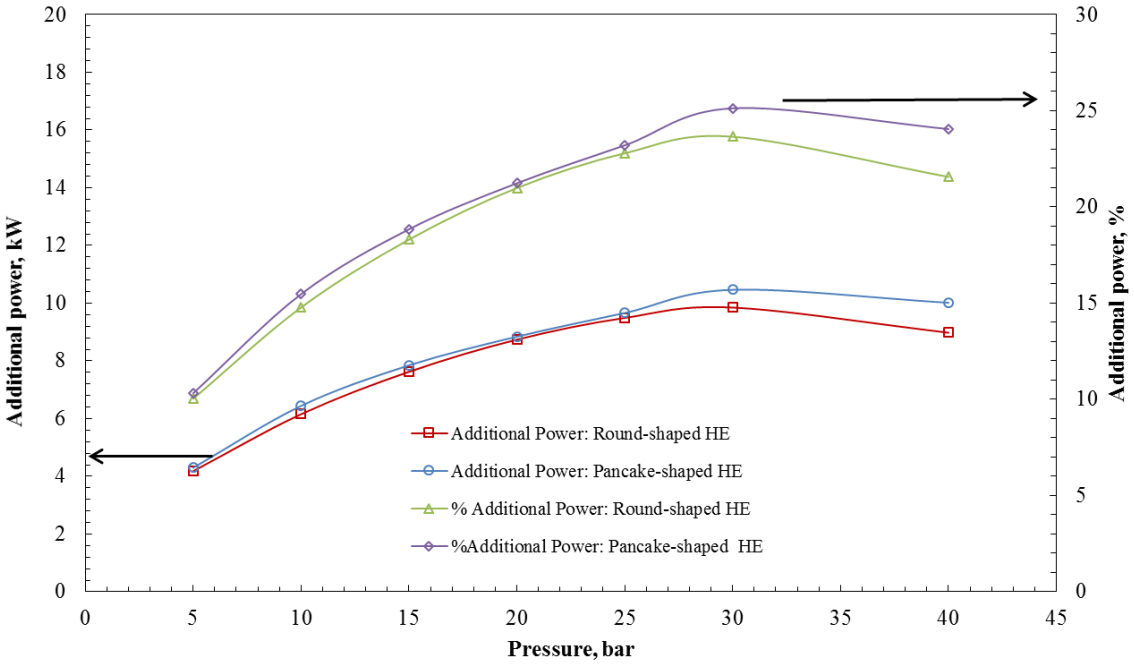

Fig. 5: Additional power generation at various working pressure.

These additional powers were calculated assuming conservative turbine efficiency of 70% [24, 25]. These additional powers resulted into 23.6% and 25.1% additional power generation by round-shaped and pancake-shaped heat exchangers, respectively. The working pressure of the working fluid at the maximum additional power was found to be 30 bar for both heat exchangers.

4. Conclusion

The exhaust of a diesel engine contains 40% of the input energy and usually this energy is wasted by expelling to the atmosphere. The overall efficiency of the diesel engine can be improved by recovering this waste heat to produce additional power by turbine using RC. In this research, optimized heat exchangers were designed to be retrofitted into vehicle. The following outcomes were established from this research:

- Pancake-shaped heat exchanger was able to generate 10.5 kW additional power whereas, round-shaped heat exchanger was able to produce 9.8 kW. The round-shaped heat exchagers were not suitable in vehicle operation because of the space limitations. However, round-shaped heat exchangers are easy to manufacture and relatively easy to clean. They can be used in diesel engine based generators.
- The improvements of power of pancake-shaped and round-shaped heat exchangers were 25.1% and 23.6%, respectivley.
- The additional power varies with the working pressure of the working fluid and the optimum pressures for both the pancake- and round-shaped heat exchangers were found to be 30 bar.

Acknowledgements

The authors gratefully acknowledge the financial and other support received for this project from the Leartek Pty Ltd.

References

[1] M. Kanoglu, S. KazIm IsIk, and A. Abusoglu, "Performance characteristics of a Diesel engine power plant," *Energy Conversion and Management,* vol. 46, pp. 1692-1702, 2005.

[2] M. Hatazawa, H., Sugita, T.,Ogawa, Y.,Seo, "Performance of a thermoacoustic sound wave generator driven with waste heat of automobile gasoline engine," *Transactions of the Japan Society of Mechanical Engineers (Part B,* vol. 70, pp. 292–299, 2004.

[3] V. Pandiyarajan, M. Chinna Pandian, E. Malan, R. Velraj, and R. V. Seeniraj, "Experimental investigation on heat recovery from diesel engine exhaust using finned shell and tube heat exchanger and thermal storage system," *Applied Energy,* vol. 88, pp. 77-87, 2011.

[4] S. Bari, "Investigation into the deteriorated performance of diesel engine after prolonged use of vegetable oil," in *ASME Internal Combustion Engine Division 2004 Fall Technical Conference*, 2004, pp. 1-9.

[5] S. Bari and M. M. Roy, "Prospect of rice bran oil as alernative to diesel fuel," in *Fifth International Conference on Small Engines, their Fuels and the Environment*, 1995, pp. 31-36.

[6] T. Lim, S. Bari, and C. Yu, "Using crude palm oil (CPO) as diesel engine fuel," *ASEAN JOURNAL ON SCIENCE AND TECHNOLOGY FOR DEVELOPMENT,* vol. 19, pp. 1-14, 2002.

[7] S. Bari, "Performance, combustion and emission tests of a metro-bus running on biodiesel-ULSD blended (B20) fuel," *Applied Energy,* vol. 124, pp. 35-43, 7/1/ 2014.

[8] M. He, X. Zhang, K. Zeng, and K. Gao, "A combined thermodynamic cycle used for waste heat recovery of internal combustion engine," *Energy,* vol. 36, pp. 6821-6829, 2011.

[9] A. Ibrahim and S. Bari, "Effect of Varying Compression Ratio on a Natural Gas SI Engine Performance in the Presence of EGR," *Energy & Fuels,* vol. 23, pp. 4949-4956, 2009/10/15 2009.

[10] A. Ibrahim, S. Bari, and F. Bruno, "A Study on EGR Utilization in Natural Gas SI Engines Using a Two-Zone Combustion Model," SAE Technical Paper2007.

[11] S. Jiangzhou, R. Z. Wang, Y. Z. Lu, Y. X. Xu, and J. Y. Wu, "Experimental study on locomotive driver cabin adsorption air conditioning prototype machine," *Energy Conversion and Management,* vol. 46, pp. 1655-1665, 2005.

[12] T. C. Hung, M. S. Shai, and B. S. Pei, "Cogeneration approach for near shore internal combustion power plants applied to seawater desalination," *Energy Conversion and Management,* vol. 44, pp. 1259-1273, 2003.

[13] P. Diehl, F. Haubner, S. Klopstein, and F. Koch, "Exhaust heat recovery system for modern cars," *SAE TRANSACTIONS,* vol. 110, pp. 988-998, 2001.

[14] D. T. Hountalas, G. C. Mavropoulos, C. Katsanos, and W. Knecht, "Improvement of bottoming cycle efficiency and heat rejection for HD truck applications by utilization of EGR and CAC heat," *Energy Conversion and Management,* vol. 53, pp. 19-32, 2012.
[15] J. Holman, "Heat Transfer, 8 th," ed: McGraw-Hill Book Company (UK) Ltd., London, England, 1997.
[16] D. Hountalas, C. Katsanos, D. Kouremenos, and E. Rogdakis, "Study of available exhaust gas heat recovery technologies for HD diesel engine applications," *International Journal of Alternative Propulsion,* vol. 1, pp. 228-249, 2007.
[17] D. Hountalas and G. Mavropoulos, "Potential for Improving HD Diesel Truck Engine Fuel Consumption Using Exhaust Heat Recovery Techniques," 2010.
[18] S. N. Hossain and S. Bari, "Waste heat recovery from the exhaust of a diesel generator using Rankine Cycle," *Energy Conversion and Management,* vol. 75, pp. 141-151, 11// 2013.
[19] "Ansys CFX-Solver Theory Guide," Release 13.0 ed: Ansys Inc., 2012.
[20] K. J. Bell, "Heat exchangers: Thermal-hydraulic fundamentals and design," *Delaware Method for Shell Side Design,* pp. 581-618, 1981.
[21] Y. G. Lei, Y. L. He, P. Chu, and R. Li, "Design and optimization of heat exchangers with helical baffles," *Chemical Engineering Science,* vol. 63, pp. 4386-4395, 2008.
[22] A. Bahadori, "Simple method for estimation of effectiveness in one tube pass and one shell pass counter-flow heat exchangers," *Applied Energy,* vol. 88, pp. 4191-4196, 2011.
[23] J. Guo, M. Xu, and L. Cheng, "The application of field synergy number in shell-and-tube heat exchanger optimization design," *Applied energy,* vol. 86, pp. 2079-2087, 2009.
[24] Y. A. Cengel, R. H. Turner, and J. M. Cimbala, *Fundamentals of Thermal-Fluid Sciences*, 3rd ed.: McGrawHill, 2008.
[25] M. J. Moran and H. N. Shapiro, *Fundamentals of Engineeering Thermodynamics*, 4th ed. USA: John Wiley & Sons, 2000.

Available online at www.sciencedirect.com

ScienceDirect

Procedia Engineering 00 (2015) 000–000

Procedia Engineering

www.elsevier.com/locate/procedia

6th BSME International Conference on Thermal Engineering (ICTE 2014)

Simulation of improvements to in-cylinder mixing of biodiesel with air by incorporating guide vanes into the air intake system

S. Bari*, P. J. G. Johansen, A. J. T. Alherz

Barbara Hardy Institute, School of Engineering, University of South Australia, Mawson Lakes Campus, SA 5095, Australia.

Abstract

Engine manufacturers and consumers around the world are concerned for the fuel efficiency and ecological footprint of their engines, and this concern has motivated increased production and usage of alternative fuels. Biodiesel is renewable and behaves similarly to diesel in an engine. Further, the emission of carbon dioxide from burning biodiesel in engines is offset by the consumption of carbon dioxide by the plant producing biodiesel feed stock. Biodiesel does, however, have an undesirable higher viscosity, larger and heavier molecules which lead to slower atomisation and less mixing with air, resulting lower combustion efficiency. To mitigate these problems, this paper proposes a guide vane swirl and tumble device (GVSTD) to be installed within the intake port for the purpose of increasing the turbulence of the air flow into the cylinder and to aid the atomisation and mixing of the biodiesel molecules with air.

Peer-review under responsibility of organizing committee of the 6th BSME International Conference on Thermal Engineering (ICTE 2014).

Keywords: Guide vanes; Biodiesel; Compression ignition engine; Air-fuel mixing

1. Introduction

Biodiesel is produced by a process called trans-esterification from source materials such as animal fats and/or vegetable oils [1-4]. This process produces a biodiesel made of methyl esters of high molecular size. Because biodiesel

* Corresponding author. Tel: +61-8-8302-3439; fax: +61-8-8302-3380.
E-mail address: saiful.bari@unisa.edu.au

Peer-review under responsibility of organizing committee of the 6th BSME International Conference on Thermal Engineering (ICTE 2014).

can be sourced from renewable crops, and has similar behaviour to petrodiesel, it can be used in existing CI engines with no modification, as demonstrated by Diesel in 1900 [1, 3, 5]. Though the use of some biodiesel blends does increase carbon dioxide emissions, they are offset by the carbon dioxide consumed by photosynthesis within the crop while it is growing [4, 6, 7]. Testing by various researchers has shown that the viscosity of biodiesel is much higher than that of petrodiesel [3, 4, 8]. This property of biodiesel is due in part to its large molecular size and weight. This higher viscosity, in conjunction with lower calorific value of the fuel, leads to a reduction in many performance parameters of engines fuelled by biodiesels, including less torque, less power, and greater fuel consumption [1, 3, 4, 8-11]. Many means of improving biodiesel's viscosity have been previously attempted, including blending biodiesel with petrodiesel [8], heating the biodiesel before injecting into the engine [10], and combinations of both methods [11]. These improvements have met with mixed results.

Increasing swirl and tumble in the in-cylinder air flow is one method of increasing the rate of evaporation and mixing of fuel into air. Swirl is defined as rotational flow about the vertical axis of the cylinder [12-14], and tumble is defined as rotational flow about an axis perpendicular to the vertical axis of the cylinder [15]. Cross tumble is defined as rotational flow about an axis perpendicular to both the swirl and tumble axes [15]. Swirl, tumble, and cross tumble can be incorporated into the in-cylinder air flow by installing vanes or shrouds in the air flow prior to the inlet valve. This article proposes a guide vane swirl and tumble device (GVSTD) to be installed in the intake runner of a compression ignition (CI) engine. It is intended to force the incoming air to conform to a swirling and tumbling pattern as it flows into the cylinder. This swirling pattern is expected to combine with the swirl generated by the piston bowl [12]. Improved swirl and tumble within the air flow at the fuel injection area between the start of injection (SOI) and start of combustion (SOC) is expected to aid the mixing of biodiesel and air, and the increased air velocity in the injection area is expected to impart velocity to the molecules of biodiesel. This swirling vortex of air will result in better air and fuel mixing and higher combustion efficiency [16]. This article will present the results of simulations of the air and biodiesel flows within cylinders for engines with and without the GVSTD, in order to assess the effectiveness of the device. The vanes of the device will be curved longitudinally. Thermal and fluid flow analyses using computational fluid dynamics (CFD) simulations are used to predict and optimize the behaviour of the products before being manufactured and this reduces the need for costly prototypes resulting saving time and costs [17-20]. However, the major shortcoming of simulations is to take into account all the parameters that might affect the results. Therefore, in this study the results of the simulations will be compared to other research in this field, in order to validate and assess the GVSTD.

2. Simulation setup

The effects of curved vanes on swirl, tumble, and turbulent kinetic energy in the air flow needed to be tested against the already established effects of flat vanes demonstrated by Saad [5]. Further, it is required that the curved vanes show an improvement over having no vanes at all, and that the effects found within the simulations can be validated by referencing against known data. Therefore, it was decided that three configurations should be simulated: an engine with no vanes running on diesel, a simulation with no vanes running on biodiesel, and a simulation with curved vanes running on biodiesel.

Table 1. (a) Specification of GVSTD; (b) Specification of engine model

(a)

Parameters	Value
Number of vanes	4
Length of vane (L)	30 mm
Width of vane	0.5 mm
Height of vane	5 mm
Vane twist angle (θ)	40° clockwise
Angle of incidence (β)	90°
Radius of curvature (r)	20 mm

(b)

Parameter	Value
Bore	104 mm
Stroke	108 mm
Compression ratio	17.9
Type of piston head	bowl in-cylinder
Engine speed	1500 rpm
Induction system	Naturally aspirated
Start of fuel injection	14° CA before TDC

Large vane surface area is indicated by the literature to produce greater swirl within the air flow [21-24]. The corollary is that larger vanes will create higher resistance to air flow [24, 25]. Increasing vane size will generate much momentum in the air flow, but simultaneously reduce volumetric efficiency. Analysis of many vane shapes and their relation to this trade-off has led to investigating the effect of axially curved vanes on air flow and fuel injection. Axially curved vanes are hypothesised to restrict air flow in a radial direction, and instead forcing it to remain constrained to the profile of the vane. In this study, there will be four vanes, equally spaced around the circumference of the air inlet runner. The design has been illustrated in Table 1a and Figure 1a.

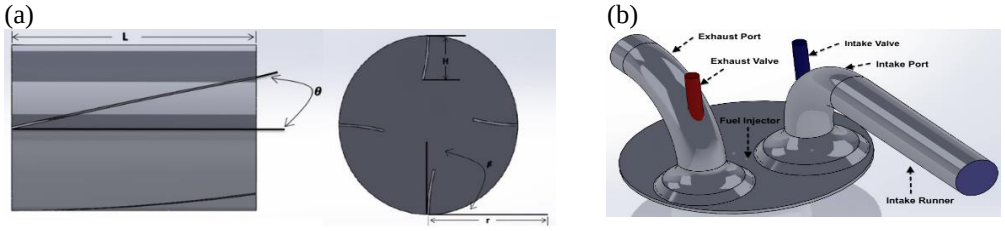

Figure 1. (a) Schematic diagram of guide vanes; (b) The drawing of the simulation model

The geometry of the simulation was based upon that of the HINO W04D diesel engine, rotating at 1500 revolutions per minute. The specifications of this engine may be seen in Table 1b. The intake valve, exhaust valve, and the fluid domain were modelled using Solidworks 2012. The empty space surrounding the fluid domain and valves is taken by the simulation to represent the aluminium engine block. The layout of the simulated engine geometry can be seen in Figure 1b. Injection timing was set to start at 706 degrees, and finish at 719 degrees, upon the recommendation of Heywood [12]. For the fuels involved in the simulation, properties were obtained from different sources. The properties of petro-diesel were sourced from the default ANSYS materials properties for diesel. The properties of biodiesel were modeled upon the biodiesel analysed by Benjumea [3]. The temperature of the injected fuel was set to 80^{o} C. The key difference between the fuels is viscosity, which will determine how the fuel departs from the ideal cone shaped injection pattern. The viscosity of the diesel was 0.0024 kg/m-s while the viscosity of the biodiesel was 0.00407 kg/m-s, giving a viscosity ratio of 1.69.

The equations used to find the solution include the continuity equation, energy and momentum equation, and the Navier Stokes equations [26]. The k-ε turbulence model was used to calculate the turbulent kinetic energy and its dissipation [27]. Iterative equations were considered complete at 100 iterations or a convergence factor of $1x10^{-4}$. Boundary conditions of the simulation were set to emulate real world conditions as closely as practicable. The air pressure and temperature inside the cylinder were set to one atmosphere and 300 K, respectively. The air inlet temperature was set to 300 K also, and the inlet and outlet air pressures were set to 1 atm. The number of time steps per crank angle in the simulation had to be set such that the convergence of the solution at each step was ensured, while not requiring excessive calculation time. Four time steps per crank angle was selected to satisfy these criteria. The number of iterations per time step was decided upon using similar criteria, and a value of 100 was chosen.

3. Results and discussion

In order to study the characteristics of the in-cylinder air flow, the results of in-cylinder pressure and temperature, swirl, tumble, cross tumble, turbulence kinetic energy (TKE) and penetration length are presented. The observation of these parameters started from 10^{o} crank angle (CA) before SOI until 10^{o} CA after top dead centre (TDC).

3.1 In-cylinder pressure and temperature

In-cylinder pressure plays key role for improving the combustion efficiency, as higher in-cylinder pressure assists evaporation and mixing of the fuel with air by increasing the volumetric efficiency. Figure 2a shows the curve of maximum in-cylinder pressure for diesel with no vanes, biodiesel with no vanes, and biodiesel with curved vanes from

10º CA before SOI to 10º CA after TDC, a time period encompassing the full fuel injection period. From the graph the curved vanes produce more in-cylinder pressure than the other models. The maximum in-cylinder pressure is about 1.004% higher with the GVSTD than without it. It is believed that an increase of pressure will result in higher volumetric efficiency of the engine. Research [28-30] investigated the effects of increased pressure, and found that it leads to improved atomisation and dispersion of the fuel molecules within the air. Further, the method of improving the in-cylinder pressure by modifying the geometry of an engine, as this paper does, was demonstrated by Miles [31] who had high in-cylinder pressure resulting from helical throttling in the intake port. Therefore, it may be said that having a guide vane in the intake runner of a CI engine should improve the mixing process.

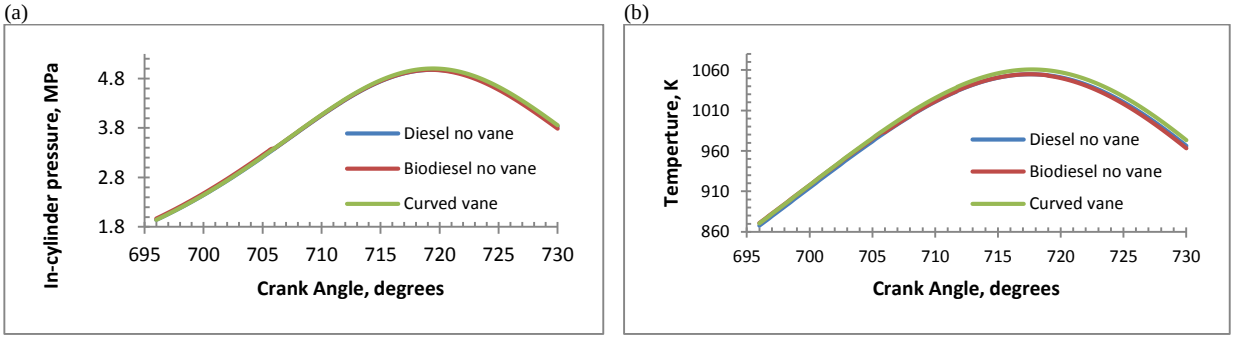

Figure 2. (a) Maximum in-cylinder pressure curve for the three models; (b) Maximum in-cylinder temperature curve for the three models

The same argument applies for in-cylinder temperature, as when the in-cylinder pressure increases, the in-cylinder temperature will increase as well. The increased temperature also leads to a higher rate of fuel vaporization [12, 32]. Higher temperature air was found in the model with the GVSTD installed, as seen in Figure 2b. In fact the curved vane resulted in a higher in-cylinder peak temperature of 1061 K than both biodiesel and diesel with no vanes which reached a peak temperature of 1055 K.

3.2 Swirl, tumble and cross tumble

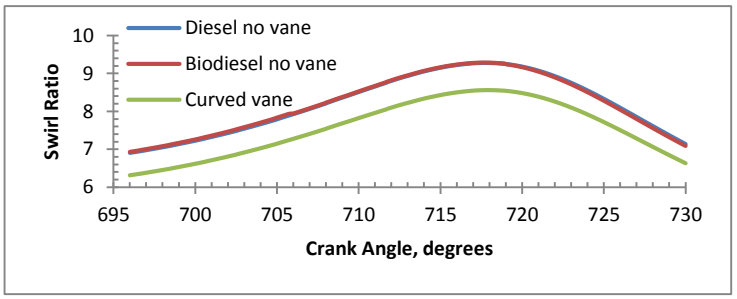

Figure 3. Swirl ratio versus crank angle for all models

Figure 3 shows the value of swirl ratio versus crank angle for the three models. The swirl ratio is defined as the ratio of rotational air flow about the swirl axis relative to the flow about the other axes. Higher in-cylinder swirl ratios can result better mixing of fuel with air and improve the engine performance [33-36]. Because the swirl ratio is determined solely by air flow characteristics, the difference between the two vane-less simulations should be minimal prior to SOI, and this is evidenced in Figure 3. However, installing vanes inside air intake runner showed a reduction of swirl values compared with CI engine with no vanes. Modifying the geometry of the intake system to increase swirl may not result better rotation of air flow, particularly if the vanes are too thick. Sometimes values of swirl are similar or slightly better than unmodified CI engine as reported by Ramadan [37] who investigated shrouding intake valves.

Ramadan tested six cases and his last case showed similar pattern of swirl at the beginning of the crank angle, followed by a slight increase in swirl, compared to the original CI engine design [42]. Moreover, swirl ratio changes are always concurrent with changes in tumble and cross tumble ratios, which are defined below.

The tumble ratio is defined as the ratio of rotational air flow about the tumble axis relative to the flow about the other axes, while the cross tumble ratio is defined as the ratio of rotational air flow about the cross tumble axis relative to the other axes. The effect of tumble or cross tumble are similar to the effect of swirl, in that a higher ratio of tumble and/or cross tumble would create more turbulence and assist mixing of fuel with air. Whether a swirl, tumble or cross tumble ratio is positive or negative is arbitrary, the important value is the magnitude of the ratio. Figures 4a and 4b present tumble and cross tumble ratios respectively for each of the models tested. Though the tumble and cross tumble ratio values for the model with vanes are initially less than the engines without vanes, the ratios quickly overtake the engine without vanes. This implies a stronger lateral flow of air within the cylinder. This lateral flow will assist in spreading the injected fuel throughout the cylinder, as explained below.

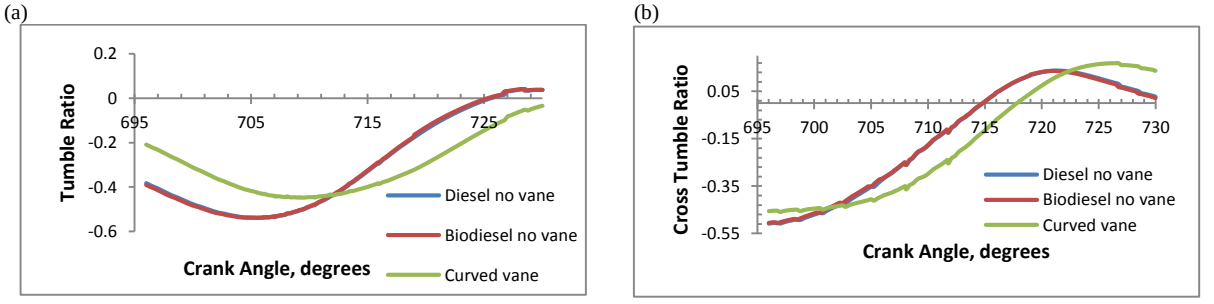

Figure 4. (a) Tumble ratio versus crank angle for all models; (b) Cross tumble ratio versus crank angle for all models

3.3 TKE

TKE is the mean kinetic energy per unit mass that is associated with eddies in turbulent flow [38]. Higher in-cylinder TKE can aid the atomisation of the fuel flow. Atomisation expands the area of air-fuel mixture with less penetration length of injected fuel and wide cone angle [1]. Higher TKE would lead to smoother and more efficient combustion, and reduced carbon deposits on engine components [12, 39]. Figure 5a illustrates TKE for all models. In-cylinder TKE during fuel injection declines almost linearly in each simulation. Research by Payri et al [40] and Saad et al [34] show similar patterns of TKE in their investigations of in-cylinder flow. Therefore the results that were obtained are in appropriate agreement. The impact of GVSTD on TKE during fuel injection was slightly less than the models with no vanes. This is to be expected, as not all vane designs are guaranteed to improve TKE, and some designs will be detrimental. Saad et al [34] tested TKE values in 10 vane designs and compared the results with an unobstructed intake runner, and four out of the 10 test showed a reduction of TKE. So, it is believed if more curved vane designs are tested, eventually some designs will result in better TKE than a design with no vanes.

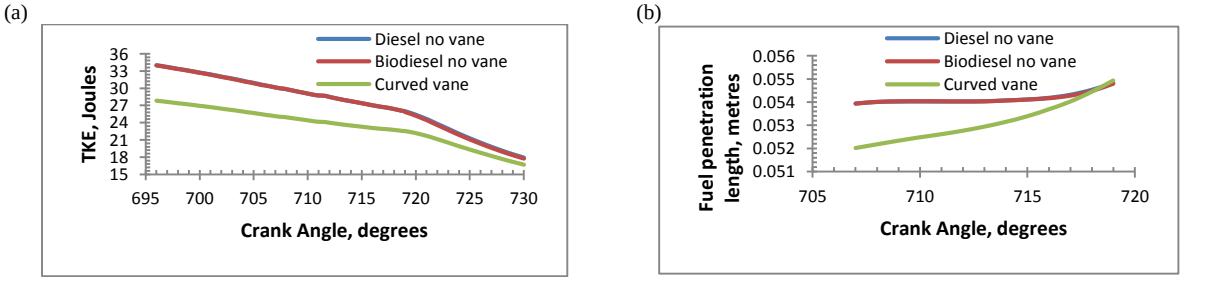

Figure 5. (a) In-cylinder TKE; (b) Penetration length for the three models during injection time

3.4 Penetration length and cone angle

As mentioned in the introduction, an optimum penetration length and wide cone angle can make a large surface area between fuel and air which will give a good evaporation and mixing of the fuel into the air. Figure 5b shows the injection penetration length for diesel and biodiesel with no vanes and curved vane simulation fuelled with biodiesel. There is a slight difference between the penetration lengths of the biodiesel and the diesel injections for the simulations without vanes, and this is attributed to the difference between fuel viscosities. The difference between the simulations with vanes and without vanes is attributed to the difference in air flow characteristics. As illustrated in Figure 5b, adding the GVSTD reduces the penetration length of the fuel initially, but the injection length then increases rapidly before TDC. This implies a longer fuel injection cone, and therefore a larger surface area for the fuel to mix with the air. The rate of length increase for the model with vanes shows that the addition of vanes allows for a much more rapid penetration, even if it is initially sluggish. The initially slow injection of fuel for the engine with vanes means that in the early periods of injection the fuel is mixing with air in the higher parts of the cylinder, while the lower parts of the cylinder are not touched by the fuel until slightly later. This slower acceleration of the fuel from the injector should therefore allow for more even mixing through the cylinder. It is a concern, however, that the increased penetration length may lead to unwanted carbon deposits on the piston bowl.

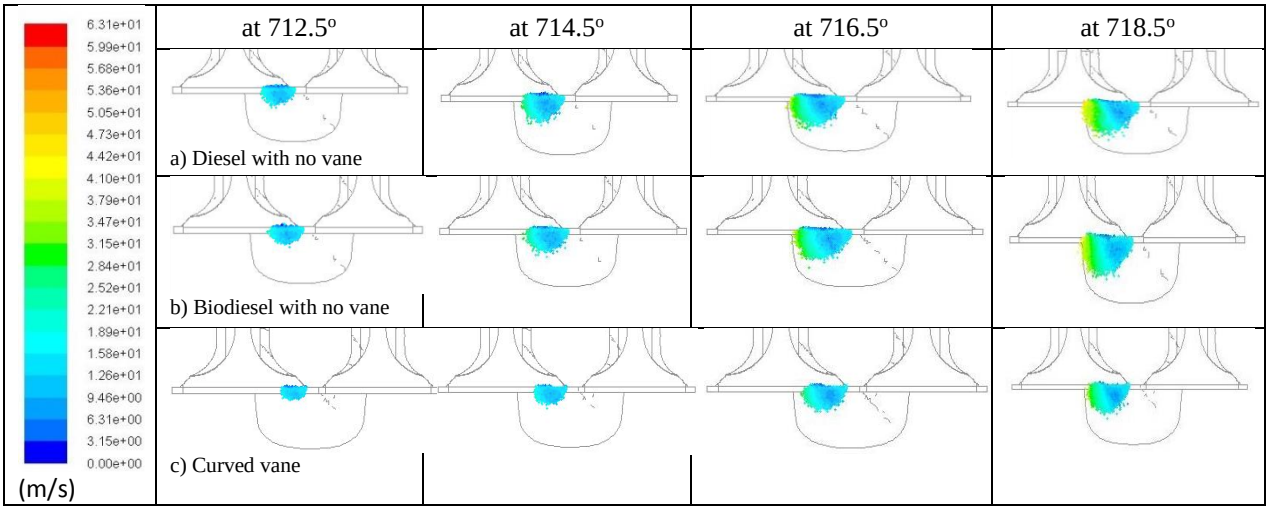

Figure 6. The injection spray and velocity of the three models at four different crank angles

Figure 6 shows the injection spray of the three models at four different crank angles. Fuel injection starts at 706º CA and ends at 719 º CA. As the initial fuel spray is minute, it was decided to start from 712.5º CA. The figure includes the velocity of injected fuel particles. Looking at Figure 6, fuel spray is pushed to the left; this is a result of the positive cross tumble values for each simulation, which will push the air in an anti-clockwise direction. The diesel has wider cone angle and good penetration length. However, the biodiesel with no vane has slightly less penetration length and less wide angle than diesel. Unfortunately, installing guide vane resulted in reduction of the spray cone angle compared with models with no vanes. Therefore, this resulted in biodiesel fuel to have a small surface area of the fuel and air which may lead to less mixing, diffusion and evaporation. It is believed that the occurrence of small surface of fuel injection is related to the low value of TKE [34, 41]. Kim et al [41] investigated in-cylinder TKE by using swirl control valves and reported that in-cylinder TKE increases will reduce fuel penetration length and the impingement of the fuel against piston head. To confirm their results, they used flame visualization and analyses of images. Based on that, the lower value of TKE that curved vane exerted and the result would be high penetration length. Moreover, as explained previously, investigation of geometry modification of CI engines done by Saad et al [34] and Payri et al [40], some of their results recorded low TKE. Therefore, it is believed that simulating other models of curved vanes would result in better TKE which would lead to reduction of fuel penetration length.

4. Conclusion

This project presented research on the effects of air flow swirl and tumble, and fuel viscosity on the behaviour of injected fuels in a CI engine. With biodiesel, in-cylinder pressure and temperature were higher with the curved vane model than without vanes and this resulted in broadly different mixing of fuel with air. The tumble and cross tumble were higher with curved vanes than without vanes. This indeed assisted in spreading the injected fuel throughout the cylinder. The TKE for curved vane model was lower than the models with no vane, although TKE was highly dependent on the shape of the vanes tested. Adding the GVSTD reduces the penetration length of the fuel initially, but the injection length then increased rapidly before TDC. This suggests that including the GVSTD will increase fuel dispersion in the cylinder. However, increased injection length may lead to unwanted carbon deposits on the piston bowl. Further, the cone angle was narrower and not wider when the GVSTD was installed.

The GVSTD shows promise as a way of altering the air-fuel mixing of CI engines powered by renewable, carbon neutral fuel, with no additional energy input required. The effects that can be achieved have been investigated preliminarily in this research, but further research is required to refine and optimize the effects of installing guide vanes in the air inlet. The further research should include the determination of how modification of individual geometric properties, such as vane length, radius of curvature, thickness, et cetera, will affect the in-cylinder air flow. The effects of each geometric change should also be tested for both diesel and biodiesel. Altering the length of the vane is expected to impart a greater change of momentum on the air flow, so it shall be considered as the next avenue of investigation.

References

[1] A. Murugesan, C. Umarani, R. Subramanian, N. Nedunchezhian, Bio-diesel as an alternative fuel for diesel engines—A review, Renewable and Sustainable Energy Reviews, 13 (2009) 653-662.
[2] S. Bari, Performance, combustion and emission tests of a metro-bus running on biodiesel-ULSD blended (B20) fuel, Applied Energy, 124 (2014) 35-43.
[3] P. Benjumea, J. Agudelo, A. Agudelo, Basic properties of palm oil biodiesel–diesel blends, Fuel, 87 (2008) 2069-2075.
[4] C. Carraretto, A. Macor, A. Mirandola, A. Stoppato, S. Tonon, Biodiesel as alternative fuel: Experimental analysis and energetic evaluations, Energy, 29 (2004) 2195-2211.
[5] I. Saad, S. Bari, Effects of Guide Vane Swirl and Tumble Device (GVSTD) to the Air Flow of Naturally Aspirated CI Engine, in: International Conference on Mechanical Engineering 2011 (ICME2011), Progressive Printers Pvt. Ltd., Dhaka, Bangladesh, 2011.
[6] C.L. Peterson, T. Hustrulid, Carbon cycle for rapeseed oil biodiesel fuels, Biomass and Bioenergy, 14 (1998) 91-101.
[7] S. Bari, M.M. Roy, Prospect of rice bran oil as alernative to diesel fuel, in: Fifth International Conference on Small Engines, their Fuels and the Environment, 1995, pp. 31-36.
[8] A. Ramadhas, C. Muraleedharan, S. Jayaraj, Performance and emission evaluation of a diesel engine fueled with methyl esters of rubber seed oil, Renewable energy, 30 (2005) 1789-1800.
[9] Y. Sharma, B. Singh, Development of biodiesel: current scenario, Renewable and Sustainable Energy Reviews, 13 (2009) 1646-1651.
[10] D. Agarwal, A.K. Agarwal, Performance and emissions characteristics of Jatropha oil (preheated and blends) in a direct injection compression ignition engine, Applied thermal engineering, 27 (2007) 2314-2323.
[11] S. Bari, Investigation into the deteriorated performance of diesel engine after prolonged use of vegetable oil, in: ASME Internal Combustion Engine Division 2004 Fall Technical Conference, ASME, 2004, pp. 1-9.
[12] J.B. Heywood, Internal Combustion Engines Fundamentals, McGraw Hill International, 1988.
[13] P. Lakshminarayanan, Y.V. Aghav, Modelling diesel combustion, Springer, 2010.
[14] J. Naser, A. Gosman, Flow Prediction in an Axisymmetric Inlet Valve/Port Assembly Using Variants of k—ε, Proceedings of the Institution of Mechanical Engineers, Part D: Journal of Automobile Engineering, 209 (1995) 57-69.
[15] J. Martins, B.S. Ribeiro, S. Teixeira, In-cylinder swirl analysis of different strategies on over-expanded cyclies,

(2009).
[16] J. Hart, J. Naser, P. Witt, Aerodynamics of an isolated slot-burner from a tangentially-fired boiler, Applied Mathematical Modelling, 33 (2009) 3756-3767.
[17] J. Hart, J. Naser, P. Witt, Coherent structure dynamics in jets from irregular shaped nozzles, in: 15th Australasian Fluid Mechanics Conference, Sydney, Australia, 2004, pp. 1-4.
[18] M.F. Rahaman, S. Bari, D. Veale, Flow investigation of the product fill valve of filling machine for packaging liquid products, Journal of food engineering, 85 (2008) 252-258.
[19] S. Bari, J. Naser, Simulation of airflow and pollution levels caused by severe traffic jam in a road tunnel, Tunnelling and Underground Space Technology, 25 (2010) 70-77.
[20] J. HART, J. NASER, P. WITT, L. MITTONI, Numerical modelling of isothermal burner jets, in: Second International Conference on CFD in the Minerals and Process Industries, 1999.
[21] J.S. Kim, Fluid Swirling Device for an Internal Combustion Engine, in: United States Patent, USA, 2003.
[22] J.S. Kim, Fluid Swirling Device, in: United States Patent, USA, 2006.
[23] K.-H. Lo, Air swirling device, in, Google Patents, 2006.
[24] S.-S. Lin, J.-C. Yang, Intake swirl enhancing structure for internal combustion engine, in, Google Patents, 2000.
[25] S.Y. Kim, Air flow system for internal combustion engine, in, Google Patents, 1999.
[26] ANSYS INC, ANSYS Fluent Theory Guide, in: R.B.F. Flow (Ed.), 2014.
[27] ANSYS INC, ANSYS Fluent Theory Guide, R. 15.0: Standard RNG and Realizable k-e Model, in, 2014.
[28] O. Nwafor, G. Rice, A. Ogbonna, Effect of advanced injection timing on the performance of rapeseed oil in diesel engines, Renewable Energy, 21 (2000) 433-444.
[29] L. Labecki, A. Cairns, J. Xia, A. Megaritis, H. Zhao, L. Ganippa, Combustion and emission of rapeseed oil blends in diesel engine, Applied Energy, 95 (2012) 139-146.
[30] R. Chowdary, M.M. Krishna, T. Reddy, P. Murthy, Performance evaluation of a high grade low heat rejection diesel engine with waste fried vegetable oil, International Journal of Engineering and Technology, 2 (2012).
[31] P.C. Miles, The influence of swirl on HSDI diesel combustion at moderate speed and load, SAE International Journal, (2000).
[32] A. Ibrahim, S. Bari, Effect of Varying Compression Ratio on a Natural Gas SI Engine Performance in the Presence of EGR, Energy & Fuels, 23 (2009) 4949-4956.
[33] S. Bari, I. Saad, CFD modelling of the effect of guide vane swirl and tumble device to generate better in-cylinder air flow in a CI engine fuelled by biodiesel, Computers & Fluids, 84 (2013) 262-269.
[34] I. Saad, S. Bari, S.N. Hossain, In-Cylinder Air Flow Characteristics Generated by Guide Vane Swirl and Tumble Device to Improve Air-Fuel Mixing in Diesel Engine Using Biodiesel, Procedia Engineering, 56 (2013) 363-368.
[35] B.M. Krishna, A. Bijucherian, J. Mallikarjuna, Effect of intake manifold inclination on intake valve flow characteristics of a single cylinder engine using particle image velocimetry, International Journal of Engineering and Applied Sciences, 6 (2010).
[36] B. Paul, V. Ganesan, Flow field development in a direct injection diesel engine with different manifolds, International Journal of Engineering, Science and Technology, 2 (2010) 80-91.
[37] B. Ramadan, A Study of Swirl Generation in DI Engines Using KIVA-3V, Kettering University, (2003).
[38] F.M. White, Fluid mechanics, 1994, in, McGraw-Hill Inc, 1979.
[39] W.W. Pulkrabek, Engineering fundamentals of the internal combustion engine, Prentice Hall Upper Saddle River, NJ, 1997.
[40] F. Payri, J. Benajes, X. Margot, A. Gil, CFD modeling of the in-cylinder flow in direct-injection Diesel engines, Computers & fluids, 33 (2004) 995-1021.
[41] K. Kim, J. Chung, K. Lee, K. Lee, Investigation of the swirl effect on diffusion flame in a direct-injection (DI) diesel engine using image processing technology, Energy & Fuels, 22 (2008) 3687-3694.

Performance Study on Effect of Rotating Vaneless Diffuser due to Blade Trimming by 10% to its vane length of Impeller in a Centrifugal Compressor Stage

Seralathan Sivamani (India), Roy Chowdhury D G (India)

Abstract

In the stationary vaneless diffuser, the sidewalls are stationary. A simplest and effective way of reducing the shear losses on the stationary vaneless diffuser sidewalls, with probable improved efficiency and flow range of low-to-medium specific speed stages, is the use of a "rotating diffuser". In the rotating vaneless diffuser, the dynamic head and the path length of the flow causing the shear losses are a function of the magnitude and direction of the relative velocity in the diffuser, which is much smaller and more radial than the absolute velocity. A particular type of rotating vanless diffuser, 'forced' rotating vaneless diffuser, in which the diffuser rotates at the speed equals that of the impeller, which is created by "blade cutback". Blade cutback involves blade trimming but leaving shroud and hub disk as it is. The extending impeller disks forms a rotating vaneless diffuser. The experimental investigations by Govardhan et al [1] and Lindner [2] reported advantages of the rotating vaneless diffuser with the small cutback rate in achieving an additional static pressure recovery. Recently, Seralathan et al. [3] studied the effect of blade cutback on a centrifugal compressor stage by trimming the blades by 5% with respect to its vane length. Matching peak efficiency was obtained at design flow coefficient for BCB05 as well as SVD. This paper is a part of the series of investigations conducted to understand the fluid mechanics behind this concept. The objective is to study computationally the effect of blade cutback on the flow diffusion along with the performance characteristics and flow parameters of a centrifugal compressor stage involving rotating vaneless diffuser. The comparative studies are carried out involving a shrouded impeller having blade cutback by 10% to its vane length (BCB10) and another shrouded impeller (SVD), both with stationary vaneless diffusers in the downstream. ANSYS ICEMCFD 13.0 is used for computational domain modeling and grid generation. Unstructured tetrahedral elements with flat prism shaped cells in the near wall zones are used to obtain a finer resolution in the boundary layer. Numerical investigations are carried out using ANSYS CFX 13.0. The turbulence was modeled using k-ω model. Flow through various diffuser configurations (BCB10 and SVD) are analyzed at design and above design conditions. Results are presented for efficiency, energy coefficient, static pressure recovery coefficient, stagnation pressure loss coefficient, absolute velocity, meridional velocity, flow angle, tangential velocity, static pressure and stagnation pressure. The matching peak efficiency is achieved at design flow coefficient for both SVD and BCB10 and slightly lesser efficiencies for off-design conditions with above design flow coefficients. The performance characteristics of BCB10 are lesser in terms of energy coefficient, specific work, as well as static pressure rise. Losses in BCB10 are higher than the SVD which is also reflected with higher stagnation pressure loss coefficient. This shows that the larger cutback have a detrimental effect on the performances with increased losses and reduced static pressure rise which is due to the adverse effect caused by the change in blade tip geometry at exit. References [1] Govardhan, M., Moorthy, B.S.N., Gopalakrishnan, G., 1978, A Preliminary Report on the Rotating Vaneless Diffuser for a Centrifugal Impeller. Proceedings of the First International Conference on Centrifugal Compressor, Indian Institute of Technology Madras, India. [2] Linder, P., 1983, Aerodynamic Tests on Centrifugal Process Compressors – Influence of Diffuser Diameter Ratio, Axial Stage Pitch and Impeller Cutback. ASME Journal of Engineering for Power, Vol. 105, pp. 910 – 919. [3] Seralathan, S., Roy Chowdhury, D.G., 2013, Computational Study on the Effect of Blade Cutback on the Performance of the Centrifugal Compressor, Procedia Technology, Vol. 10, pp. 400-408.

Keywords: centrifugal impeller, extended shroud, blade cutback, rotating vaneless diffuser, stationary vaneless diffuser

Available online at www.sciencedirect.com

ScienceDirect

Procedia Engineering 00 (2015) 000–000

Procedia Engineering

www.elsevier.com/locate/procedia

6th BSME International Conference on Thermal Engineering (ICTE 2014)

Modeling the Energy Extraction from In-stream Water by Multi Stage Blade System of Cross Flow Micro Hydro Turbine

Shahidul, M. I, Syed Tarmizi,S.S, Abdullah Yassin, Al Khalid Othman, Hushairi Zen, Ting Ching Hung, and Lee Man Djun*

Faculty of Engineering, Universiti Malaysia Sarawak.Malaysia

Abstract

This paper aims to present energy extraction behavior of multi stage Micro Hydro Turbine (MHT), particularly when it operates in a low velocity In-Stream water body. Development a MHT with multi stage blade (runner) for water velocity ranges from 0.5 m/s to 1.0 m/s is the novelty of this research. Findings of literature review on MHT and simulation results of ANSYS CFD software are the basis of designing this research project. The vital parameters involved in designing the turbine were blade area, blade stage, blades position against water flow direction, spacing between blades, blade materials; and other technical factors associated with turbine operations. The study revealed that the turbine had started to extract energy at water velocity 0.3 m/s at 35 RPM turbine speed. At water inlet velocity 1.1 m/s, the velocity drop across blade was 25.6% and the energy extraction efficiency was 48.3%. The findings demonstrated that the energy extraction capacity of turbine blade had been greatly influenced by the blade stages and water velocity. The study concludes that the developed turbine is useful in low velocity In-stream water body for energy extraction and would be able to contribute to achieve energy and environmental sustainability.

Peer-review under responsibility of organizing committee of the 6th BSME International Conference on Thermal Engineering (ICTE 2014).

Keywords: Water Velocity; Energy Extraction; Turbine Speed; Multi Stage; Turbine Performance

1. Introduction and background of research

Various types of Micro Hydro turbine (MHT) are available in the market and generally all are operated on water velocity more than 1 m/s , even energy extraction efficiency of these turbines is less than 50 percent ($\eta \leqslant 50\%$). The

* M. Shahidul Islam. Tel.: +6-082-583-282
E-mail address: mislam@feng.unimas.my

Peer-review under responsibility of organizing committee of the 6th BSME International Conference on Thermal Engineering (ICTE 2014).

traditional MHT is manufactured with one set blade (single stage); while the water velocity in major percentage of the river is less than 1 m/s which reduces the scope of using available MHT. Ultimately, people living in those areas where water velocity less than 1 m/s they have no choice. To address this issue, the current research project has been undertaken.

Nomenclature

V_i	inlet water velocity
V_o	outlet water velocity
RPM	turbine rotation per minutes
E	energy extraction
Ps	shaft power
A	blade area
ρ	water density
ΔV	water velocity drop
A	blade area of turbine

1.1. Literature Review

Micro-hydro projects are becoming popular due to society's need for generating electricity without the fossil fuel cost. MHT converts kinetic and potential energy of running water into electrical energy through turbine blades and generator. Most large scale hydro turbines are installed at dams to ensure maximum power output. In contrast, most in-stream micro hydro extracts energy directly from the mainstream. The efficiency of most MHT founds in a range of 30 to 40% [1]. The micro hydro system is suitable for "run-of-the-river" installations. As dam is not required to operate in-stream micro hydro systems, the capital cost of this type of turbine is less compared to the large scale hydro systems [2]. The latest studies on micro hydro system suggest that this technology is reliable and friendly to environment compare to other sources of energy. It also provides a solution to energy supply for remote and hilly areas where the extension of grid system is not economically and technically feasible [3, 4].

Based on the alignment of the rotor axis with respect to water flow, this turbine family has been divided into two main groups, namely, axial flow and cross flow. The axial flow turbine has an axis parallel to water flow; on the other hand the power transmission shaft of the cross flow turbine is vertical to water flow. Cross flow water (CFW) turbine has been divided into two groups such as vertical axis and in-plane axis. The energy transmission shaft of the vertical axis turbine is vertical to water plane, and other hand, the shaft of in-plane axis turbine is installed parallel to water flow. Examples for vertical axis turbine are SC-Darrieus, H-Darrieus, Darrieus, Gorlov and Savonius. Indeed, in the operational phase of vertical axis turbine some disadvantages have been observed such as low starting torque, torque ripple, and lower efficiency [5].

In regards to CFW turbine, Verdant Power had made a test report on operations and they stated that energy extraction by CFW turbine depends on water velocity and effective area of turbine blade [6]. For example, New Energy Corporation manufactured a turbine, their test report had indicated that it produced 13.0 kW at water velocity 2.5 m/s. Similar report had been made by Thropton Energy Service, they found that their manufactured turbine had produced 2 kW at water velocity 1.5 m/s. These results proved that the power extraction depends on water velocity. Alternative Hydro Solutions LTD and GCK Technology Inc. had produced a few turbines with blade area 3.0 sqm and 1.0 sqm respectively. The output power of these turbines was 2.6 kW and 0.7 kW respectively, though the water velocity for both cases were 1.4 m/s and 1.3 m/s respectively. These findings have proved that turbine blade area can play a significant role in extracting energy from water [7, 8]. However, nowadays research efforts have been given to use End Suction Centrifugal Pump Operating in Turbine Mode for Micro hydro Applications in order to increase energy extraction efficiency [9].

1.2. Theoretical framework for energy extraction by using multistage blade system

Optimizing the energy extraction is the key objective of this research project. To achieve this goal, a mechanical devise is essential to maximize velocity drop across the turbine blades [10]. In order to increase energy extraction efficiency, the outlet water velocity (V_o) at the turbine exit must be minimized; and to achieve this condition, the water velocity drop across the blades must be maximized. Therefore, the challenge of this research project is to increase velocity drop (V_o) across the blade surface.

1.2.1. Conceptual energy flow modelling

A conceptual model of energy extraction and conversion to mechanical energy of MHT is shown in Fig.1.

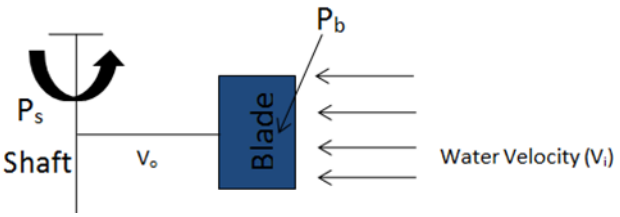

Fig.1: conceptual model of energy extraction by turbine blades

Fig.1 demonstrates that the inlet water velocity (V_i) is passed over the blade surface. At the exit the blade surface, water velocity V_i is reduced to Vo (Vo <Vi). The difference between V_i -V_o is known as velocity drop across turbine blades. The velocity drop is considered the scale of energy extraction. Therefore, the interaction maximization between water and blade surface is the determinant of energy extraction.

1.2.2. Modeling the energy extraction by using multistage blade system

The energy available in flowing water [11] can be presented by equation (1):

$$E = \frac{\rho C A V^3}{2} \quad (1)$$

Here, E is energy; A is the blade area contact with flowing water, C = Power coefficient, V = water velocity m/s at inlet point and ρ water density (kg/m^3) at normal atmosphere conditions. This equation indicates that blade area is a dominant factor of energy extraction. Another important factor of energy extortion is water velocity drop across blades of a turbine. The energy extraction with respect to velocity drop is shown by Eq.2:

$$\Delta E = E_i \_ Eo$$
$$\Delta E = 1/2\rho CA(vi^3 \_ vo^3) \quad (2)$$

The energy extraction in percent can be estimated from the equation (3):

$$\Delta E\% = \frac{\mathrm{Ei}-\mathrm{E0}}{\mathrm{Ei}}100$$

$$\Delta E\% = \frac{Vi^3 - Vo^3}{V^3}100 \quad (3)$$

1.2.3. Modeling the velocity drop

In a study on MHT, M.L. Arena found that the velocity drop in a single stage turbine is about 33% [8]. It indicates, in the single stage turbine, water leaves turbine with a huge amount of energy. In that study also reported that velocity

drop at turbine blades can be increased by increasing the stages of blades. This concept can be represented by Eq.4:

$$\Delta V=\sum_1^5 \Delta Vi \quad (4)$$

$Here, \Delta V$ - The velocity drop at each blade stage, i=1,2,3,4 and 5. Number 5 indicates number of stage of blade.

1.2.4. Modeling the blade area for energy extraction

The basic model of energy extraction indicates, Eq.1, that it can be maximized by increasing the interaction between blade surface and water flux. On the other hands, if blade surface increases and splits in different stages, it could provide better scope of kinetic energy utilization. This scenario is shown in Fig. 2 and Eq.5.

$$A = \sum_1^5 Ai \quad (5)$$

$Here, A$ - The total blade area of MHT. i=1,2,3,4 and 5. Number 5 indicates number of stage of blade.

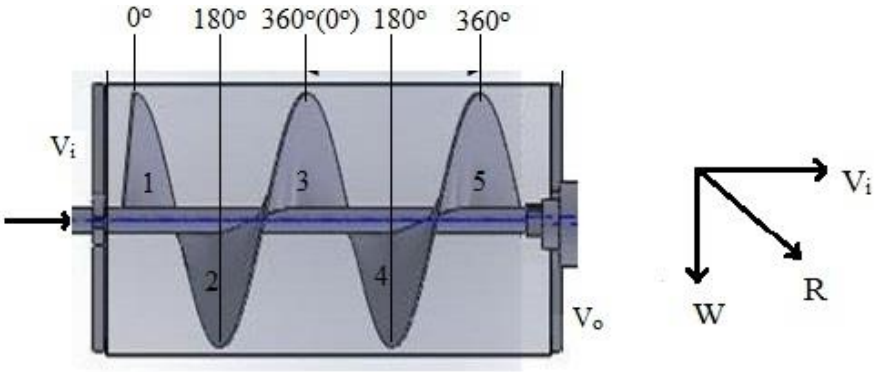

Fig. 2: turbine blade assembly

The energy vector shown in Fig. 2 indicates that R is the reactive force and it is generated during water flow over the blades. The magnitude of 'R' depends on the amount of velocity drop over the blade surface and this force contributes to rotating turbine shaft.

2. Research problem statement and objectives

Since available MHT is not useful for low-velocity water (v ≤1 m/s) and the fact is that a major percentage of people in rural area are being lived nearby water stream having velocity about 1.0 m/s. It implies that people's house around low velocity water area are not able to use existing and readily available MHT. Moreover, energy extraction efficiency of available MHT is less than 40%. In order to address this issue, current research project has undertaken. The focus of this research project is to develop a MHT suitable to operate at water velocity ranges from 0.3 m/s to 1.0 m/s with higher energy extraction efficiency. Particularly, we pay attention to develop multistage blade (runner) design; because we are convinced by the aid of literature that proposed system will be able to increase velocity drop.

2.1. Novelty of the research

Report on MHT with multistage blade design in series for low-velocity water turbine is not available in the literature; hence a gap exists in this field. This work has designed to fill-up this gap. In this background, developing the multi stage blade (runner) for water velocity ranges from 0.3 m/s to 1.0 m/s is novel.

2.2. Research objectives

The broad objective of this study is to determine the effect of multistage blade and water velocity on energy extraction of MHT. The specific objectives of this study are:

- To estimate energy extraction
- To evaluate velocity drop across turbine blades
- To determine turbine RPM

3. Research methodology

The study on multistage MHT begins with the literature review for collecting latest research findings. The conceptual model building was the second stage of research. Designing and developing laboratory scale turbine was the third stage of this research. The final stage was conducting experiments to validate the developed model.

3.1 Scope of study and research design

Five stages laboratory scale MHT has designed and developed to conduct study. The selected inlet water velocity ranges was from 0.3m/s to 1.0 m/s. To achieve research objectives, we measure inlet (V_i) and outlet (V_o) water velocity and speed (RPM).

3.1 Experiment setup and data collection

The layout and machinery setup are shown in Fig.3. The main equipments associate with experiment were water channel, variable speed water pump, water flow piping system, five stage horizontal type cross flow turbine ,energy transfer pulley and alternator.

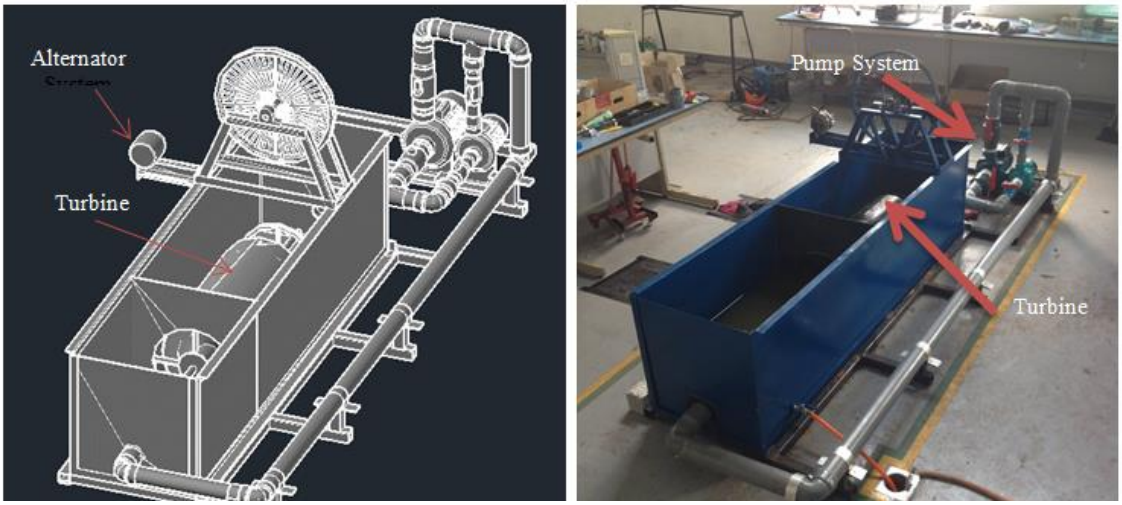

Fig. 3. experimental setup

Two centrifugal pumps had used to maintain water flow. Water flow rate and water velocity had egulared by using frequency inverter. Two veleicty meters had used to measure inlet and outlet water velecity. One hand drive techcometer had used to measure turbine speed (RPM). The total operating time of machinery was 240 hours in different working days. Five sets data (0.3m/s, 0.5m/s, 0.7m/s, 0.9m/s and 1.1 m/s) have gathered from experiments. In order to reduce estimating error and achieving higher data quality, statistical technique, SPSS software had used. The data only within 3 standard deviations (3σ) had used for analysis.

4. Turbine test and data analysis

Laboratory scale MHT has been installed in a water channel (Fig.3) and test run has been conducted at various water velocity. Eq. 3 and Eq.4 were estimated to evaluate energy extraction and velocity drop. The findings of turbine operation are reported in Table 1 and pictured in Fig. 4.

Table 1. Laboratory scale turbine test date and result

V_i (m/s)	V_o (m/s)	ΔV (%)	E (%)	RPM
0.3	0.270	12	18.3	35
0.50	0.292	16	40.78	45
0.70	0.437	17.5	43.5	67
0.90	0.71	20.35	44.5	120
1.1	0.752	25.6	48.3	150

Here, ΔV is velocity drop across blades and E is energy extraction from water by blades.

Table 1 demonstrates the impact of velocity drop on energy extraction. It is evident that at water velocity 0.3 m/s, the velocity drop was 12 percent across blades; the extracted energy efficiency was 18.3 percent and the shaft speed was 35 RPM. It was observed that the energy extraction was increased further with velocity drop. At water velocity 1.1 meter/s, the velocity drop was 25.6 percent and the extracted energy efficiency was 48.3 percent with shaft speed 150 RPM. It was also observed that the rotation of the turbine was also increased with velocity drop. The characteristics of energy extraction and velocity drop with respect to inlet velocity are shown in Fig. 4(a) and Fig. 4(b).

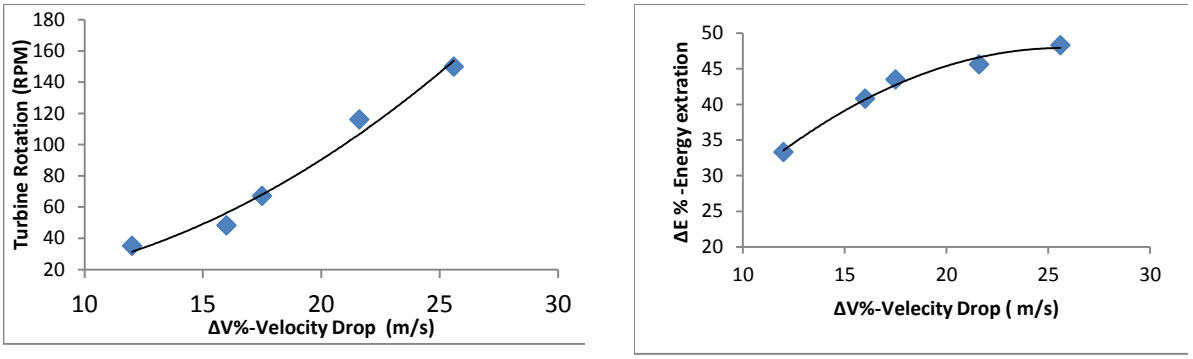

Fig 4. (a) Effect of velocity drop on turbine rotation; (b) effect of velocity drop on energy extraction

Fig.4 (a) and Fig.4 (b) demonstrate the nature of energy extraction and turbine speed with respect to velocity drop. Relevant equations are shown below:

$$\Delta E\% = 4.15\Delta V - 0.81\Delta V^2 - 4.69 \quad (6)$$

$$RPM = 12.237 + 0.29\Delta V^2 - 1.88 \quad (7)$$

Equation (6) and (7) can be used to predict energy extraction of low water velocity turbine.

5. Research findings and scenario analysis

This study has estimated the energy extraction efficiency of multistage micro hydro turbine at low water velocity. The energy extraction at water inlet velocity 0.3 m/s was 18.3 percent which was the lowest value in this experiment. The maximum energy extraction was 48.3 percent at water inlet velocity 1.1 m/s. These findings demonstrate that turbine rotation and energy extraction depend on water velocity drop. The turbine speed 35 RPM was insignificantly low and at this speed energy extraction was also minimum. The water velocity 0.9 m/s and 1.1 m/s appeared useful to extract energy from water because at that water velocity the turbine speed were 120 RPM and 150 RPM. Indeed, velocity drop across turbine blade and the energy extraction were also significantly higher and compare able to other

research findings [3, 8]. Based on these experimental findings, it could be stated that multistage blade system is able to extract energy at about 1.0 m/s water velocity. Thus, this study has achieved its research goal.

5.1. Practical implication of research findings

In-stream multistage blade MHT is a useful machine for extracting low cost energy from water; and the model reported in this paper would be greatly useful in increasing its efficiency. These findings would insist policy makers for commercializing this turbine. The developed turbine would also be commercially feasible for manufacturing SMEs, agriculture projects and residence nearby river for boost up economy.

5.2. Social implication of research findings

Approach used in this study would be an effective way of extracting higher percentage energy from in-stream water and also to increase turbine operating performance; Of course, higher energy extraction performance would contribute to increase environmental sustainability; thus society would be benefited by using developed model.

5.3. Conclusion and direction for further study

Findings of this study suggest that multistage MHT has power to contribute to increase energy extraction efficiency at lower water velocity. This study concludes that the developed model would be greatly useful in future research for developing commercially feasible micro hydro turbine. The future direction of research would be to characterize energy extraction at water velocity more 1.0 m/s. Another direction for future study is to model energy extraction with more than 5 stage of blades.

Acknowledgements

Authors would like to acknowledge the financial supports received from ministry of higher education Malaysia under FRGS grant (ref FRGS/TK01(01)973/2013). Authors are pleased offer special thanks to academic staff of Engineering Faculty, Universiti Malaysia Sarawak. Authors are pleased to express their gratitude to Prof. Dr. A.K.M. Sadrul Islam for encouragement to undertake this research back in 2000.

Reference

[1] A.Z.A. Majid, N. Shaari, S.B.M. Yusoff. Design Approach for Customers Experience in Services, 3rd Int. Conf. on Applied and Creative Arts 2011, Universiti Malaysia Sarawak, 2011. ISBN 978-967-5224-75-1.

[2] D. Hislop. Energy Options: An Introduction to Small-Scale Renewable Energy Technologies, Intermediate Technology Publications, London, UK, 1992.

[3] M.I. Shahidul, A.R.H.Rigit, R.S. Hafiza, M.L. Arena, A.H. Ruduan. Optimization of Energy Extraction from Low Speed Water Current: Application of Ducted Cross-Flow Turbine, ASEAN Australian Engineering Congress, 2011.

[4] R. Nathan, H. Ibrahim, P. Kumaran. Micro hydro potential in West Malaysia, International Conference of Energy and Environment, 2009, pp. 348-359.

[5] Hydrovolt, Inc. In-stream hydrokinetic turbines. Retrieved September 21, 2010 from http://www.hydrovolts.com/MainPages/Hydrokinetic%20Turbines.htm

[6] Verdant Power Canada ULC. Technology Evaluation of Existing and Emerging Technologies: Water Current Turbines for River Applications. Verdang Power, Canada, 2006.

[7] Alternative Hydro Solution. Development of Darrieus Turbines: Alternative Hydro Solutions. Retrieved May 2, 2012 from http://www.althydrosolutions.com/development.html.

[8] M.L. Arena. Dynamic Operating Behaviour of In-Stream Cross Flow Micro Hydro Turbine, Master thesis for Master Degree of Engineering, Mechanical and Manufacturing Engineering Department, Universiti Malaysia Sarawak, 2012.

[9] M.A.Ismail, Al Khalid Othman, M.I. Shahidul Islam, Z.Hushairi, 'End Suction Centrifugal Pump Operating in Turbine Mode for Microhydro Applications'Hindawi Publishing Corporation Advances in Mechanical Engineering Volume 2014, Article ID 139868, 1-7 pages, http://dx.doi.org/10.1155/2014/139868

[10] H. Cowan, R. Harmon. The market case for green energy: a multiple perspective approach. PICMET Proceedings:2498, Portland, 2007.

[11] G. Hagerman, B. Polagye. Methodology for estimating tidal current energy resources and power production by tidal in-stream energy conversion (TISEC) devices, EPRI North American Tidal In Stream Power Feasibility Demonstration Project, Rev. 3, pp. 1-55, 2006.